



First analysis of the $\nu_2 + \nu_7$ and $\nu_2 + \nu_9$ and $\nu_2 + \nu_6$ combination bands of HNO₃: evidence of perturbations due to large amplitude OH torsion in the 2 1 9 1 excited state

A. Perrin, L. Manceron, R. Armante, F. Kwabia-Tchana, P. Roy, D. Doizi

► To cite this version:

A. Perrin, L. Manceron, R. Armante, F. Kwabia-Tchana, P. Roy, et al.. First analysis of the $\nu_2 + \nu_7$ and $\nu_2 + \nu_9$ and $\nu_2 + \nu_6$ combination bands of HNO₃: evidence of perturbations due to large amplitude OH torsion in the 2 1 9 1 excited state. Molecular Physics, 2021, 10.1080/00268976.2021.1987543 . hal-03384913

HAL Id: hal-03384913

<https://hal.science/hal-03384913>

Submitted on 22 Oct 2021

HAL is a multi-disciplinary open access archive for the deposit and dissemination of scientific research documents, whether they are published or not. The documents may come from teaching and research institutions in France or abroad, or from public or private research centers.

L'archive ouverte pluridisciplinaire **HAL**, est destinée au dépôt et à la diffusion de documents scientifiques de niveau recherche, publiés ou non, émanant des établissements d'enseignement et de recherche français ou étrangers, des laboratoires publics ou privés.

20/09/2021

First analysis of the $\nu_2+\nu_7$ and $\nu_2+\nu_9$ and $\nu_2+\nu_6$ combination bands of HNO_3 : evidence of perturbations due to large amplitude OH torsion in the 2^19^1 excited state.

A. Perrin^{a,*}L. Manceron^{b,c},R. Armante^aF. Kwabia-Tchana^d,P. Roy^bD. Doizi^e

^aLaboratoire de Météorologie Dynamique/IPSL, UMR CNRS 8539, Ecole Polytechnique, Université Paris-Saclay, RD36, 91128 Palaiseau Cedex, France

^b Ligne AILES, Synchrotron SOLEIL, L'Orme des Merisiers, St-Aubin BP48, 91192 Gif-sur-Yvette Cedex, France.

^c Sorbonne Université, CNRS, MONARIS, UMR 8233, 4 place Jussieu, Paris, F-75005 France

^d Université de Paris and Univ Paris Est Creteil, CNRS, LISA, F-75013 Paris, France

^e DEN-Service d'Etude du Comportement des Radionucléides (SECR), CEA, Université Paris-Saclay, F-91191, Gif-sur-Yvette, France

20/09/2021

Number of tables: 6

Number of figures: 12

* Corresponding author: agnes.perrin@lmd.ipsl.fr,

For Peer Review Only

20/09/2021

Abstract:

This paper is the first of two back-to-back works, whose goal is to update the existing line positions and intensities spectroscopic parameters for the 5.8 μm region of nitric acid in the HITRAN or GEISA spectroscopic databases. This first study is devoted to the generation of first linelists for the $\nu_2+\nu_9-\nu_9$, $\nu_2+\nu_7-\nu_7$, and $\nu_2+\nu_6-\nu_6$ hot bands in the 5.8 μm region, while the second study will concern the positions and intensities for the ν_2 band centered at 1709.567 cm^{-1} . High resolution Fourier transform spectra were recorded in the 5.8 μm and in the 4.2 – 4.6 μm spectral ranges. The identification of the $\nu_2+\nu_9$, $\nu_2+\nu_7$, and $\nu_2+\nu_6$ bands of HNO_3 at 2165.0036 cm^{-1} , 2285.9657 cm^{-1} and 2351.216 cm^{-1} , respectively, was performed, and several assignments were confirmed by searching for $\nu_2+\nu_9-\nu_9$ and $\nu_2+\nu_7-\nu_7$ transitions within those of ν_2 at 5.8 μm . Both $\nu_2+\nu_6$ and $\nu_2+\nu_9$ bands are highly perturbed. Surprisingly, both $\nu_2+\nu_9$ and $\nu_2+\nu_9-\nu_9$ bands exhibit large amplitude torsional splittings of $\sim 0.043 \text{ cm}^{-1}$. This is presumed to be due to the existence of an anharmonic resonance that couples together the 2^19^1 energy levels with those of a dark state involving high excitation in the ν_9 large amplitude OH torsional mode.

20/09/2021

I Introduction

This paper is the first of two back-to-back works, whose goal is to update the existing line positions and intensities spectroscopic parameters for the 5.8 μm region of nitric acid in the HITRAN [1] or GEISA [2] spectroscopic databases. This paper is devoted to the first generation of linelists for the $\nu_2+\nu_9-\nu_9$, $\nu_2+\nu_7-\nu_7$, and $\nu_2+\nu_6-\nu_6$ hot bands, while the second one [3] will concern the improvement of line positions and intensities for the ν_2 cold band.

Indeed, contrary to the linelists for the other main infrared absorption band regions of nitric acid (22 μm [4], 11 μm [5, 6, 7], and 7.5 μm [8]), the 5.8 μm band is the only one for which spectroscopic parameters for hot bands are missing in spectroscopic databases. Therefore, the preliminary goal of this study was to get accurate linelists for the $\nu_2+\nu_9-\nu_9$, $\nu_2+\nu_7-\nu_7$, and $\nu_2+\nu_6-\nu_6$ hot bands centered at 1706.775 cm^{-1} , 1705.666 cm^{-1} , and 1704.416 cm^{-1} , respectively, which are associated to the ν_2 cold band at 1709.567 cm^{-1} that will be considered in the next paper [3]. Because the band centers of their lower associated states, the 9^1 , 7^1 and 6^1 vibrational states are located at 458.229 cm^{-1} , 580.304 cm^{-1} , and 646.826 cm^{-1} , respectively, the $\nu_2+\nu_9-\nu_9$, $\nu_2+\nu_7-\nu_7$, and $\nu_2+\nu_6-\nu_6$ hot bands are in the intensity ratio 0.108, 0.060 and 0.043, respectively, at 296 K. Therefore, among these hot bands, $\nu_2+\nu_9-\nu_9$ merits special attention because it leads to the strongest signature at 5.8 μm .

In the 11 μm and 7.5 μm regions, we are dealing with mainly A-type bands. In this case, most of the infrared signature of the hot bands gather into sharp Q branches, and a rather broad spectroscopic investigation can often provide a good description of these hot bands, even for a rather high resolution purpose. This is the case for the $\nu_3+\nu_9-\nu_9$ hot band located in the 7.5 μm

20/09/2021

[8], or, in the 11 μm region, for the $\nu_5+\nu_9-\nu_9$ band [5, 6] and for the $\nu_5+\nu_7-\nu_7$ and $\nu_5+\nu_6-\nu_6$ hot bands [7].

In the 5.8 μm region, we are dealing with (mainly) B- type bands and, as can be seen in Fig. 1, the contribution to the infrared absorption due to the hot bands spreads mostly over the P and R branches of the ν_2 cold band. Therefore, a high resolution analysis is required for these hot bands in order to model their infrared signature. Thus, in order to get energy level parameters (band centers and rotational constants) for the 2^19^1 , 2^17^1 and 2^16^1 vibrational states, we performed, in a first step, the identification of the $\nu_2+\nu_9$, $\nu_2+\nu_7$, and $\nu_2+\nu_6$ combination bands of HNO_3 at 2165.0036 cm^{-1} , 2285.9657 cm^{-1} and 2351.216 cm^{-1} , respectively. For these combination bands, our analyses use mainly a high-resolution Fourier transform spectrum recorded for a large value of the (pressure \times pathlength product) in the $2100 - 2450\text{ cm}^{-1}$ spectral region. The assignments were rather easy for the $\nu_2+\nu_7$ band but very difficult for both the $\nu_2+\nu_6$ and $\nu_2+\nu_9$ bands, which are perturbed. To complete the information on the 2^19^1 energy levels and confirm the existence of surprising large amplitude torsional splittings, we combined the investigation of the $\nu_2+\nu_9$ band at $4.6\text{ }\mu\text{m}$ with the analysis of the $\nu_2+\nu_9-\nu_9$ hot band P- and R- lines in a second spectrum in the $1650 - 1750\text{ cm}^{-1}$ ν_2 spectral region. Finally, let us mention that the present investigation was only partial for the very weak $\nu_2+\nu_6$ band which is severely blended by CO_2 lines. Furthermore, the $\nu_2+\nu_6$ assignments could not be confirmed by searching for lines belonging to the $\nu_2+\nu_6-\nu_6$ hot band which is very weak at $5.8\text{ }\mu\text{m}$.

II Experimental details.

20/09/2021

High-resolution spectra of HNO_3 were recorded with the Bruker IFS125HR Fourier transform spectrometer of the AILES Beamline at Synchrotron SOLEIL (Saint-Aubin, France). As HNO_3 reacts and quickly decomposes in contact with metal or oxidizable surfaces, its handling requires special precautions and the AILES special long path glass cell made for highly corrosive or reactive species [9] was used. The cell was fitted here with wedged diamond windows (Advanced Diamond Materials, USA) mounted with Teflon™-coated silicone gaskets (Eriks, France). It includes a triple-envelope glass body (Verrerie Soufflée Normalisée, France) with an inner volume of about 14 liters (15 cm ID \times 80 cm length) surrounded by an annular cylindrical space for circulating cold ethanol and a third envelope for the insulating vacuum (5×10^{-5} hPa). The gas temperature was measured in four different points of the cell by PTFE-coated Pt-100 sensors, corresponding to both ends and to middle top and bottom. The pressure was measured using a Pfeiffer 10 hPa capacitive gauge. The metal parts in contact with gas were coated with a thick PTFE layer (STIM, France) and the mirrors were mounted on Teflon™ bellows (Elkinger, Germany) allowing for travel and tilt adjustments. The cell uses a simple White-configuration with gold coated mirrors with a special Al_2O_3 solid protective layer (Optimask, France). The optical path length was set to 2.72 m for the ν_2 region around 5.8 μm (FTS2 in Table 1) and set to 16.32 m for the 4.6 μm region (FTS 262729 in Table 1). These spectra were recorded at 296 K and 250K, respectively.

For the 5.8 μm region (FTS2), the interferometer was used with a globar source and a 1.15 mm diameter aperture. It was equipped with a Ge/KBr beamsplitter and a homemade 4K-cooled detector with cold 1160-1900 cm^{-1} bandpass filter (Spectrogon, UK) and devoted electronics [10]. Interferograms were acquired without apodization at 80 kHz scanner fringe frequency and a maximum optical path difference (MOPD) of 530 cm. According to the Bruker definition (resolution = $0.9/\text{MOPD}$), this corresponds to a resolution of 0.0017 cm^{-1} and thus a full width at half maximum of the apparatus sinc function of about 0.0012 cm^{-1} , thus always narrower than the Doppler width (ca. 0.0025 cm^{-1}). 368 interferograms were averaged in 16 blocks (30 min) over 12 h (total duration). In this way, the small HNO_3 pressure decrease could be assessed from the decrease of HNO_3 lines and translated in pressure variation and, next, uncertainty. When the HNO_3 lines showed a noticeable change

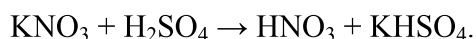
20/09/2021

(<10%) and the NO₂ lines grew in, the cell was evacuated and slowly refilled by keeping the sample in a low temperature bath at -52°C until the initial pressure was reproduced.

For the 4.6 μm region (FTS262729), the interferometer was used with a 1 mm diameter aperture, an InSb detector at 77 K and a MOPD of 300 cm, giving a full width at half maximum of the apparatus sinc function of about 0.0022 cm⁻¹, thus narrower than the Doppler width (ca. 0.003 cm⁻¹). 480 scans were averaged in 8 blocks for a 8 h measurement duration, during which the HNO₃ sample was continuously maintained at -40°C in order to keep a constant vapor pressure in the cell. To avoid build-up of NO₂ with time, the gas sample was pumped and replenished each hour.

The spectra were calibrated by matching the measured positions of either residual H₂O or CO₂, CO or N₂O to reference wavenumbers available in HITRAN [1] with a root mean square (RMS) deviation of 1.8×10⁻⁴ cm⁻¹. Given the good precision of the reference lines, it is safe to claim a 3 ×10⁻⁴ cm⁻¹ frequency accuracy for the strong lines which are used for the calibration, or for the ν₂ lines in the 5.8 μm region. However, for most of the weak or blended lines which are considered during the present analyses, the frequency accuracy is only of ~1 ×10⁻³ cm⁻¹

High purity HNO₃ was synthesized in the laboratory and kept at low temperature. Chemical syntheses were carried out under vacuum using a glass apparatus equipped with PTFE-sealed stopcocks [11]. Glass tubes, also with PTFE-sealed stopcocks, were connected to the apparatus via PTFE fittings and were used for trapping, evaporating, and storing samples at liquid nitrogen temperature. In order to prevent any decomposition, the set-up was passivated twice with a few mbar of N₂O₅ before recording the spectrum. High purity nitric acid (HNO₃) was obtained following reaction of high purity concentrated sulfuric acid with anhydrous potassium nitrate (KNO₃) held in a 0°C bath (H₂SO₄, 99.99% purity, Sigma-Aldrich, France) [12] :



Nitric acid, a colorless liquid when of high purity, was collected into a trap at -196°C. The vapor pressure of HNO₃ was checked at 22°C (68 hPa [12]) and the sample purity was assessed spectroscopically in the mid IR. Small traces of NO₂ could be estimated to less than 0.4% in VMR after each cell filling, but grew in with time at speed increasing with the cell temperature. In the highest P×L product spectrum (1.1 hPa × 16.3 m) used to observe the

20/09/2021

combination transitions near $4.5\text{ }\mu\text{m}$, interfering CO , N_2O and CO_2 lines are conspicuously standing out over the weak HNO_3 combination lines but an estimate, based on HITRAN [1] parameters, indicates that their partial pressures are about 6×10^{-5} , 2×10^{-5} and 3×10^{-4} hPa, respectively.

The following procedure was used for measurements. A background spectrum was first recorded at a resolution of 0.02 cm^{-1} while the cell was being continuously evacuated. The infrared gas cell was then filled several times with HNO_3 vapor to make sure that the cell walls were saturated and, for the final measurements, fresh sample gas pressures were introduced slowly until the desired pressure was reached. The decrease in HNO_3 line intensities was monitored with a time resolution of one measurement block and corrected for the small amount of NO_2 appearing with time (typically up to 4×10^{-4} mbar which is the NO_2 partial pressure in the 3×10^{-2} mbar total pressure). At the end of each measurement block, the gas sample was pumped and replenished to the initial pressure. The corrected pressure values were next averaged over the whole duration. To check the consistency of our measurements, the total integrated intensity over the whole ν_2 band region was measured. The total band intensity at 296 K is found to be $5.2(3)\times 10^{-17}\text{ cm/molec.}$, to be compared to $5.71(19)\times 10^{-17}\text{ cm/molec.}$ in reference [13].

Table 1 summarizes the experimental data for the spectra used in this work. Also, Fig. 1 and Fig. 2 present an overview of the spectra recorded in the $1650\text{--}1750\text{ cm}^{-1}$ and $2140\text{--}2400\text{ cm}^{-1}$ regions, respectively. Finally, Figs. 3 to 8, and Figs. 9 and 10, provide details of the FTS262729 and FTS2 spectra, respectively.

III Method of analyses.

General considerations

20/09/2021

HNO₃ is a planar C_s type molecule, with nine vibrational modes, which, except for ν_9 (the large amplitude OH torsion relative to its –NO₂ moiety at 458.229 cm⁻¹), can be considered as “low amplitude” vibrational modes.

Due to the particular values of its rotational constants ($A \approx B \approx 2C$), two types of clustering of the $[J, K_a, K_c]$ energy levels, here identified as “K_c=d” and “K_a=d”, respectively are usually observed in infrared spectra.

- The “K_c=d” clustering occurs for energy levels involving very low K_c values ($K_c \ll K_a \approx J$), and, in this case, the $[J, K_a, K_c = J - K_a]$ and $[J, K_a, K_c = J - K_a + 1]$ levels are at the same energy.
- “K_a=d” clustering: For low or medium K_a values ($K_a \ll K_c \approx J$), the $[J, K_a = J - K_c, K_c]$ and $[J, K_a = J - K_c + 1, K_c]$ rotational levels are grouped together, and K_a is degenerated (K_a=d).

As mentioned previously, the ν_9 mode (OH torsion) is a large amplitude mode. When this effect has to be considered, the “K_a = d” clustering is lifted. This means that the ($K_a = J - K_c \Leftrightarrow K_a = J - K_c + 1$) torsional subcomponents mentioned above are split, and this torsional splitting grows, with increasing excitation in the ν_9 large amplitude torsional mode, with values going from ~ 0.0006 cm⁻¹, ~ 0.002 cm⁻¹ up to ~ 0.06 cm⁻¹ in the 9¹, 9² and 9³ vibrational states, respectively. In addition, for the $[J, K_a, K_c]$ energy levels involving very high K_a values ($K_c \ll K_a \approx J$), this large amplitude motion induces a staggering of the (even K_a versus odd K_a) levels. These effects, splittings and staggerings, were easily observable during the investigation of the 3 ν_9 - ν_9 and 3 ν_9 - ν_5 , 3 ν_9 -2 ν_9 hot bands [14]. These investigations also led to the determination of the HNO₃ torsional potential $V(\gamma)$ as a function of the torsional angle γ [14,15].

In this work, we are dealing with combination or hot bands involving in their 2¹6¹, 2¹7¹, or 2¹9¹ upper states, one quantum of excitation in the ν_2 mode (NO₂ antisymmetric stretch, at 1709.568 cm⁻¹) and one quantum in the ν_6 (O-NO₂ stretch, stretch at 646.826 cm⁻¹), ν_7 (O-NO₂ bend, at 580.304 cm⁻¹) or ν_9 (OH torsion) vibrational modes. Except for ν_9 , all these vibrational modes are of low amplitude and, because in 9¹ the torsional splittings are of

20/09/2021

only $\sim 0.0006 \text{ cm}^{-1}$, perturbations due to large amplitude effects, should not be observable during this infrared study. No torsional splitting effect was **indeed** noticed during the investigation of the $\nu_8+\nu_9$ combination band [16], or during the observation of the Q branch of the $\nu_5+\nu_9-\nu_9$ hot band [5].

According to symmetry considerations for the (usually) planar C_s - type HNO_3 molecule, $\nu_2+\nu_9$ is a C-type band, while both $\nu_2+\nu_7$ and $\nu_2+\nu_6$ are hybrid bands with both B-type and A-type transitions. However, the $\nu_2+\nu_7$ and $\nu_2+\nu_6$ bands are probably mainly A-type bands, while the $\nu_2+\nu_9-\nu_9$, $\nu_2+\nu_7-\nu_7$, and $\nu_2+\nu_6-\nu_6$ hot bands, associated to the ν_2 cold band, are (mainly) B-type bands. Let us note that, among the latters, the weaker and highly perturbed $\nu_2+\nu_6-\nu_6$ band could not be adequately identified in our spectrum at $5.8 \mu\text{m}$ because its lines are masked under stronger transitions from the ν_2 cold band.

During this work, we had to deal with A-, B-, and C-type bands for nitric acid, whose main characteristics have previously been summarized [15]. Also, it is necessary to specify which types of transitions can really be assigned, since we are dealing with rather weak combination bands ($\nu_2+\nu_6$, $\nu_2+\nu_7$ and $\nu_2+\nu_9$) or with hot bands ($\nu_2+\nu_9-\nu_9$, $\nu_2+\nu_7-\nu_7$).

- The $\nu_2+\nu_7$ and $\nu_2+\nu_6$ A –type bands at $4.37 \mu\text{m}$ and $4.25 \mu\text{m}$, respectively. The P and R branches are structured in line packets involving rather low K_a values ($0 \leq K_a \leq \sim J/2$) (or rather high K_c values). Each of these P(n) or R(n) clusters groups together lines associated with the same value of $n = (J-2 \times K_c)$, where J and K_c are the quantum numbers of the upper vibrational state. The separation of clusters is $\sim (B+C)/2$, where B and C are the rotational constants. These bands have a rather sharp Q-branch structure which groups together transitions involving very high K_a ($K_a \sim J$) values. Detailed examples are given in Figs. 3 to 6.
- Figures 7 and 8 show portions of the C-type $\nu_2+\nu_9$ band in the $4.62 \mu\text{m}$ region. The strongest transitions in the P and R branches involve rather high K_a values ($\sim J/2 \leq K_a \leq J$), and these lines are grouped in clusters involving the same J rotational quantum

20/09/2021

numbers, and the separation between two clusters is $\approx (B+C)$. Among these clusters, the transitions involving very high K_a values ($K_a \approx J$) are quite strong and can be well identified. This C-type band possesses a very sharp and congested Q branch which groups together transitions involving almost only very low K_a ($K_a \sim 0$ or 1) values.

- Figs. 9 and 10 present two detailed views of the $\nu_2+\nu_9-\nu_9$ and $\nu_2+\nu_7-\nu_7$ (B-type) hot bands at 5.8 μm . As for A-type bands, the P(n) or R(n) clusters of lines involving rather high K_c values are quite easily observable. In addition, the P and R branches include series of ($\Delta J = \Delta K_a = \pm 1$) transitions involving very high K_a values ($K_a \sim J$), with a separation of $\sim (B+C)$ between two lines of the same series. For these hot bands, the Q- type transitions ($\Delta J = 0$, $\Delta K_a = \pm 1$), which are located within the strongest ν_2 lines, could not be unambiguously identified.

Therefore, it is easy to understand that for both C-type and A-type bands, the set of rotational quantum numbers involved in the transitions observable in the P and R branches, on one hand, and in the Q branches on the other hand, are very different. Therefore, when necessary and when possible, we tried to obtain confirmations of the $\nu_2+\nu_9$ and $\nu_2+\nu_7$ assignments by searching at 5.8 μm for corresponding P or R lines of the $\nu_2+\nu_9-\nu_9$ and $\nu_2+\nu_7-\nu_7$ (B-type) hot bands. Unfortunately, this was not possible for the weak $\nu_2+\nu_6-\nu_6$ hot band.

Line position and intensity computations.

The first identifications of the very weak $\nu_2+\nu_9$, $\nu_2+\nu_6$, and $\nu_2+\nu_7$ combination bands were initiated by using predicted line lists (positions and intensities) and generated as follows.

At least during the preliminary step of the calculations, we used an A-type Watson-type rotational Hamiltonian written in I' representation (see Table 2) for the computation of the upper and lower state energy levels. In all this work, the lower state rotational levels in the ground state or in the $\nu=9^1$, 6^1 or 7^1 excited states were computed using the rotational constants of Ref. [17]. For the preliminary computation of the upper states energy levels, the

20/09/2021

values of the $2^1 9^1$, $2^1 6^1$ and $2^1 7^1$ rotational parameters were calculated from those existing in the literature for the 2^1 [18], the ground, and the 9^1 , 6^1 and 7^1 [17] states, using the following expression:

$$X_{2v} = X_2 + X_v - X_0 \quad \text{Eq.(1)}$$

Here X_2 , X_v and X_0 , with $X = A, B$ or C , are the rotational constants and the centrifugal distortion constants for the 2^1 , and the $v = 9^1, 6^1$ or 7^1 excited states and for the $v = 0$ ground state. Also, we estimated the E_{29} , E_{27} and E_{26} upper state vibrational band centers from the observation of the FTS spectrum of the v_2+v_9 , v_2+v_7 and v_2+v_6 bands. For the $2^1 9^1$, $2^1 7^1$ and $2^1 6^1$, the energy level parameters were gradually improved, when possible, during the assignment process. In addition, for the $2^1 9^1$ state, a theoretical model, briefly described in the subsection “ v_2+v_9 ” of section III and which accounts for the large amplitude torsional effect had to be used at a given step of the assignment process.

The line intensities (in $\text{cm}^{-1}/(\text{molecule} \times \text{cm}^{-2})$) at 296 K for the $\text{H}^{14}\text{N}^{16}\text{O}_3$ (main) isotopic species in a natural sample of nitric acid, were computed using the usual expression:

$$k_v^N(T) = a_{iso} \frac{8\pi^3 \tilde{\nu}}{4\pi\epsilon_0 3hc} \exp\left(-\frac{E_L}{kT}\right) \left(1 - \exp\left(\frac{hc\tilde{\nu}}{kt}\right)\right)^{-1} \frac{1}{Z(T)} R_L^U \quad \text{Eq.(2)}$$

In this expression, L and U are respectively the lower and upper levels of the transition and $\tilde{\nu} = (E_U - E_L)/hc$ is the wavenumber of the transition in cm^{-1} . Also, $a_{iso} = 0.989110$ is the isotopic concentration associated to the considered $\text{H}^{14}\text{N}^{16}\text{O}_3$ species during the computation performed for a natural sample of nitric acid. In addition, $Z(T)$ is the total partition function:

$$Z(T) = Z_{vib}(T) \times Z_{rot}(T), \quad \text{Eq.(3)}$$

which includes a vibrational $Z_{vib}(T)$ and rotational part $Z_{rot}(T)$.

During this work, we used the values

20/09/2021

$Z_{\text{vib}}(250 \text{ K}) = 1.11673$, $Z_{\text{rot}}(250 \text{ K}) = 21258.47$ and so $Z(250 \text{ K}) = 24815.80$,

$Z_{\text{vib}}(296 \text{ K}) = 1.29952$, $Z_{\text{rot}}(296 \text{ K}) = 27390.91$, and so $Z(296 \text{ K}) = 35595.09$. Eq.(4)

at 250 K and 296 K, respectively.

Finally, R_L^U is the square of the matrix element of the transformed dipole moment operator, which, for the $\nu_2+\nu_9$ bands, takes the following form:

$$R_L^U = \left| \left\langle \nu^U, J' K'_a K'_c \left| {}^{\nu U, \nu L} \mu'_Z \right| \nu^L, J'' K''_a K''_c \right\rangle \right|^2, \quad \text{Eq. (5)}$$

In this expression, ${}^{\nu U, \nu L} \mu'_Z$ is the transition moment operator associated to the considered “ νU - νL ” band.

For the three combination bands under study, the expansion of the transition operators was restricted to first order operators in $i\varphi_{y=C}$, for $\nu_2+\nu_9$, and in $\varphi_{z=A}^1$ for $\nu_2+\nu_6$ and $\nu_2+\nu_7$. For the present intensity calculation, we used the following values:

$${}^{29,0} \mu_1^C \approx 2.9 \times 10^{-3} \text{ D}, \quad {}^{26,0} \mu_1^A \approx 2. \times 10^{-3} \text{ D}, \quad \text{and} \quad {}^{27,0} \mu_1^A \approx 2.2 \times 10^{-3} \text{ D}, \quad \text{Eq. (6)}$$

for the first order terms in these transition moment expansions for the $\nu_2+\nu_9$, $\nu_2+\nu_6$, and $\nu_2+\nu_7$ bands, respectively. These values are based on our (crude) estimation of the band intensities of these very weak bands that we made according to the estimation of the HNO_3 partial pressure and of the experimental conditions adopted during the recording of the FTS262729 spectrum (see Table1). Indeed, no band intensity data exist for these three bands in the literature and, as mentioned previously, these three bands are completely masked by the noise or by CO or CO_2 lines in the PNNL cross sections [13].

¹ $i\varphi_{y=C}$, $\varphi_{x=B}$, and $\varphi_{z=A}$, are is the direction cosine between the Z- laboratory fixed and the y = C, x = B, and z = A molecular fixed axes,

20/09/2021

For the $\nu_2+\nu_6-\nu_6$, $\nu_2+\nu_7-\nu_7$ and $\nu_2+\nu_9-\nu_9$ hot bands which correspond to the $\nu_U-\nu_L = 2^1 6^1-6^1$, $2^1 7^1-7^1$, $2^1 9^1-9^1$ vibrational transitions, we assumed that the harmonic approximation holds. In such conditions, we can use for these hot bands the same expansion of the transition moment operator than for the ν_2 associated cold band:

$${}^{26,6}\mu'_Z = {}^{27,7}\mu'_Z = {}^{29,9}\mu'_Z = {}^{2,0}\mu'_Z \quad \text{Eq.(7)}$$

As mentioned in the introduction, a line intensity study was performed in parallel for lines of the ν_2 band (Ref. [3], this issue). During that study, the following expansion of the ν_2 band transition operator was obtained:

$${}^{2,0}\mu'_Z = {}^{2,0}\mu_1^B \times \varphi_x + {}^{2,0}\mu_2^B \times \varphi_x]^2 + {}^{2,0}\mu_2^A \times \varphi_z + {}^{2,0}\mu_4^A \times 1/2(\{\varphi_x, iJ_y\} + \{i\varphi_y, J_x\}) \quad \text{Eq.(8)}$$

with²

$${}^{2,0}\mu_1^B = 0.2548 \text{ D}, \quad {}^{2,0}\mu_2^B = 0.552(45) \times 10^{-5} \text{ D}, \quad {}^{2,0}\mu_2^A = 0.05739(66) \text{ D},$$

$$\text{and } {}^{2,0}\mu_4^A = -0.740(64) \times 10^{-3} \text{ D} \quad \text{Eq.(9)}$$

Assignment process

At the starting point of this analysis, we adopted the same strategy for these three combination bands. The predicted linelists helped us to perform the first assignments. The calculated ground state energy levels [17] were added to the observed line positions assigned during this work for the $\nu_2+\nu_6$, $\nu_2+\nu_7$ and $\nu_2+\nu_9$ bands, to get a preliminary set of experimental

² Values (in Debye, 1 D = 3.33564×10^{-30} C m)

20/09/2021

upper state energy levels for the 2^{19}_1 , 2^{16}_1 and 2^{17}_1 excited vibrational states. These upper state levels were then introduced in a least squares fit to get, when possible, refined values for the upper states parameters and, thus, perform next new assignments, improve the accuracy of the parameters, allowing then further new assignments. For the $\nu_2+\nu_6$ and $\nu_2+\nu_7$ bands, this iterative process was pursued until it was not possible to perform further assignments. Indeed, as will be clear later in the text, we had to adopt a different strategy for the $\nu_2+\nu_9$ band. This analysis was very easy for the $\nu_2+\nu_7$ band, and quite complicated for the strongly perturbed $\nu_2+\nu_6$ and $\nu_2+\nu_9$ bands.

IV Results

The $\nu_2+\nu_7$ band:

The analysis of the very weak $\nu_2+\nu_7$ band proved to be rather easy. Indeed, this band appeared unperturbed and it absorbs in a rather clear region of our spectrum. For this band we could perform reliable assignments for more than 600 lines in the P, Q and R branches. The observed 2^{17}_1 energy levels were introduced in a least squares computation to get rather accurate upper state vibrational and rotational parameters for the 2^{17}_1 state, which are quoted in Table 3, together with their associated uncertainties. In this way, 92.35% of the 379 observed 2^{17}_1 energy levels could be reproduced within 0.001 cm^{-1} , which is satisfactory for a very weak band.

The results of the calculation of the synthetic spectra (line positions and intensities) for the $\nu_2+\nu_7$ band are given in Table 4.

Figures 3 and 4 present respectively portions of the P and Q branches of the $\nu_2+\nu_7$ band, and it is clear that the agreement is excellent between the observed and calculated spectra.

20/09/2021

The $\nu_2+\nu_6$ band:

In our spectrum, the $\nu_2+\nu_6$ band of HNO_3 is severely overlapped by strong absorptions due to the ν_3 band of CO_2 . However, in the P and R branches, we could identify about 200 lines which, for this (mainly) A-type $\nu_2+\nu_6$ band, correspond to transitions involving low K_a values. However, it is obvious that this band is clearly perturbed and a classical Watson-type Hamiltonian cannot reproduce the observed energy levels. One consequence is that the assignments could not be pursued until very high rotational quantum numbers (only 120 energy levels with $J \leq 39$ and $K_a \leq 6$) and, in particular, that we could not perform faithful assignments of the Q branch. Furthermore, at 5.8 μm , lines from the $\nu_2+\nu_6-\nu_6$ hot band associated to the 2^16^1 state are too weak to be clearly identified within those of the ν_2 band.

We tried predicting the dark states which can be responsible for the resonances perturbing the 2^16^1 energy levels, but without success. Therefore, during the final least squares fit computation performed to get the 2^16^1 energy levels parameters, we removed the most perturbed levels from the list of 2^16^1 observed energy levels, and only the E_v band center and the A, B and C rotational constants were determined. These parameters are quoted in Table 5 together with their associated uncertainties.

The results of the calculation of the synthetic spectra (line positions and intensities) for the $\nu_2+\nu_6$ band are given in Table 4. Since the perturbations due to dark states are not accounted for during our calculation, we used, whenever possible, the observed 2^16^1 energy levels achieved in this study instead of the calculated ones during the line position calculations for the $\nu_2+\nu_6$ band and the $\nu_2+\nu_6-\nu_6$ hot band.

For transitions of the P or R branches of the $\nu_2+\nu_6$ band involving rather low rotational quantum numbers, the agreement between the observed and calculated spectra is nice, and this is evidenced in Figure 5 for the P branch in the 2345 cm^{-1} spectral region. Also, Fig. 6 gives an overview of the Q branch of the same band: it is clear that our calculation reproduces the overall structure of the $\nu_2+\nu_6$ band, but we are still unable to give a detailed general description of that band.

20/09/2021

The $\nu_2+\nu_9$ band:

The $\nu_2+\nu_9$ feature is partially overlapped by the $\nu_4+\nu_5$ band of HNO_3 at 2140.17 cm^{-1} and by the $\nu_3+\nu_5$ (and/or) $\nu_3+2\nu_9$ bands in the $2190\text{--}2230\text{ cm}^{-1}$ spectral region. Furthermore, in our spectrum, this band is also overlapped by the CO fundamental band.

During the first step of the assignments of the $\nu_2+\nu_9$ band, we could identify the (rather) strong and isolated lines in the P and R branches which correspond to transitions involving very low K_c values ($K_c \leq 1$, with $K_a = J - K_c$ and $K_a = J - K_c + 1$), and examples are given in Fig. 7. These assignments were confirmed, when possible, by the identification within the ν_2 lines at $5.8\text{ }\mu\text{m}$ of the P or R transitions of the $\nu_2+\nu_9-\nu_9$ hot band involving the same 2^19^1 upper state energy levels, and an example of this type of transition is given in Fig. 10. As for the 2^16^1 state, the observed energy levels are quite perturbed. Clearly, a classical Watson-type rotational operator fails to reproduce the observed 2^19^1 energy levels, and this situation occurs even for very low J values. To illustrate this point, we plotted as a function of $K_a = J$ in Fig. 11 the differences between the observed-calculated energy levels (Obs-Calc) for the $[J, K_a = J, K_c = 0]$ levels of 2^19^1 . For $K_a = 4\text{--}16$ the (Obs-Calc) data are positive for even K_a and negative for odd K_a . It is clear that a classical Watson-type rotational Hamiltonian cannot reproduce the observed energy levels because a staggering (even versus odd K_a values) of the $[J, J, 0]$ energy levels is observed. This indicates that perturbations due to large amplitude effects are responsible for, at least, part of the observed resonances.

Using an effective theoretical model that accounts for large amplitude OH-torsional effects for HNO_3 [8, 19], it was possible to improve the quality of the predictions for both the lines of the (cold) $\nu_2+\nu_9$ and (hot) $\nu_2+\nu_9-\nu_9$ bands and to perform new assignments. In this way, we could identify torsional splittings for transitions involving low or medium K_a values both for the (cold) $\nu_2+\nu_9$ and the (hot) $\nu_2+\nu_9-\nu_9$ bands. This is a second indication that the large amplitude effects are to be considered for the 2^19^1 energy levels. This model helped us also to identify transitions involving very low K_a values within the very congested Q branch of the $\nu_2+\nu_9$ band, and this is because these assignments could be confirmed by corresponding line assignments within the P(n) or R(n) clusters in the $\nu_2+\nu_9-\nu_9$ band. Examples of these torsional splittings are given in Figs 7 to 10. However, it is clear that additional resonances exist which affect the 2^19^1 energy levels, and this complicates the assignments. Altogether we

20/09/2021

assigned more than 884 lines (306 and 578 respectively for the $\nu_2+\nu_9-\nu_9$ and $\nu_2+\nu_9$ bands), leading to the measurements of about 517 levels of the $2^{19}1$ state.

The theoretical model used to account for the classical rotation and the large amplitude effects during the computation of the $2^{19}1$ energy levels was extensively described elsewhere [8, 19]. This Hamiltonian matrix described in Table 2 includes a torsional operator written in the IAM (Internal Axis Method) formalism [19, 20, 21, 22] together with a classical Watson-type rotational operators written in the I^r representation with an A-type reduction. This torsional operator involves the θ and φ torsional angles, which were maintained at their values achieved during the study performed for the $\{5^1, 9^2\}$ interacting states of nitric acid [19]:

$$\theta_0 = 0.97852^\circ, \quad \theta_J = 0.002649^\circ \text{ and } \varphi = 1.91197^\circ \quad \text{Eq. (10)}$$

Indeed, in Ref. [19], it proved necessary to use a J-description for $\theta(J)$:

$$\theta(J) = \theta_0 + \theta_J J(J+1) \quad \text{Eq. (11)}$$

Furthermore, it was also necessary to take into account, through a non-orthorhombic term in $h_v^0\{J_x, J_z\}$, the C-type Coriolis resonance that couples together the two torsional subcomponents.

As mentioned previously, numerous additional perturbations were observed during the investigation of the (cold) $\nu_2+\nu_9$ and (hot) $\nu_2+\nu_9-\nu_9$ bands, and we could not identify the dark states responsible for these resonances. Therefore, only a part of the observed $2^{19}1$ energy levels was introduced in a least squares fit calculation in order to obtain the parameters involved in the Hamiltonian matrix. More explicitly, the energy levels which lead to

20/09/2021

(observed- calculated) differences larger (in absolute) than 0.008 cm^{-1} were excluded from the fit. The 2^{19^1} parameters determined during such a computation are listed in Table 6, together with their associated uncertainties. The statistical analysis of the calculations, given also in Table 6, shows that the results are satisfactory, although not perfect of course because additional vibrational resonances exist, which could not be accounted for.

Fig. 12 presents the plot of the (observed – calculated) energy levels for the 2^{19^1} state as a function of the energy level values. This figure compares the results of the energy levels calculations when taking into account, or ignoring, the torsional splittings. It is clear that better agreements between the observed and calculated energy levels are achieved when the torsional splittings are accounted for. However for 2^{19^1} levels with energies such that $E[J, K_a, K_c] \geq 2350 \text{ cm}^{-1}$, it is clear that other resonances exist which, unfortunately, could not be accounted for by the present calculation. These resonances concern, first, series involving $K_a \approx 19$ and $J \geq 20$, and $K_a \approx 14$ and $J \geq 22$ rotational quantum numbers, and as expected, the density of perturbations increases with increasing energies. Unfortunately we are still unable to provide a more detailed description of the observed perturbations.

The results of the calculation of the synthetic spectra (line positions and intensities) for the $\nu_2+\nu_9$ band are described shortly in Table 4.

Fig. 7 presents a portion of the P branch of the $\nu_2+\nu_9$ band near 2148.2 cm^{-1} . The torsional splittings which concern transitions involving rather low K_a (or rather high K_c) values are quite observable. In this figure, we identify also the strong $[J, K_a, K_c = d] - [J'' = J-1, K_a'' = K_a-1, K_c'' = d]$ transitions with $K_a = J$ and $K_a = J-1$, and $K_a = J-2$.

Fig. 8 gives an overview of the Q branch of the $\nu_2+\nu_9$ band near 2164.8 cm^{-1} . The identified lines belong to the $[J, 0, J] - [J, 1, J]$ and $[J, 1, J] - [J, 0, J]$ series of transitions. The $K_a = 0 \Leftrightarrow K_a = 1$ torsional splittings are quite obvious.

20/09/2021

IV Computation of the $\nu_2+\nu_9-\nu_9$, $\nu_2+\nu_6-\nu_6$, $\nu_2+\nu_7-\nu_7$ hot bands

The linelists of the $\nu_2+\nu_9-\nu_9$, $\nu_2+\nu_6-\nu_6$, $\nu_2+\nu_7-\nu_7$ hot bands in the 5.8 μm region were computed for line positions using the band centers and rotational constants listed in Tables 3, 4, and 5 for the 2^19^1 , 2^16^1 , and 2^17^1 upper states, respectively. However, during the line position computation, the observed 2^19^1 or 2^16^1 upper state energy levels were used instead of the calculated ones. In such situations, the accuracy of line positions for the $\nu_2+\nu_7$, $\nu_2+\nu_9$ and $\nu_2+\nu_6$ transitions ranges between ~ 0.002 to $\sim 0.40\text{ cm}^{-1}$ depending if the corresponding upper state was observed or not.

Table 4 provides a short description of the lists generated in this way (number of lines, wavenumber and intensity range, total band intensities).

To check the quality of these linelists, we compared the observed and calculated spectra in different regions of the FTS2 spectrum recorded in the 5.8 μm region at 296 K. These hot lines are observable within strong ν_2 cold band lines and, for this latter, we used the line prediction that we generated simultaneously for the ν_2 band ([3], this issue).

Fig. 9 shows a portion of the P branch in the 1699 cm^{-1} spectral region. We note that the P clusters are very different for the $\nu_2+\nu_7-\nu_7$ ($P(n=15)$ and $P(14)$), as well as, for the $\nu_2+\nu_9-\nu_9$ ($P(n=17)$ and $P(n=16)$) hot bands, because of the existence torsional splittings in the 2^19^1 state.

Fig. 10 shows a portion of the R branch in the 1718.4 cm^{-1} spectral region for the $\nu_2+\nu_9-\nu_9$ hot band, where the structure of the $R(n=29)$ cluster is detailed. One transition involving very high K_a value ($K_a=J=14$ in 2^19^1) is also observable.

V Discussion

20/09/2021

There are still remaining issues, especially concerning the origin of the resonances observed during the investigation of the $\nu_2+\nu_9$ and $\nu_2+\nu_6$ bands. In fact, the number of dark vibrational states that can possibly be responsible for the resonances affecting the 2^16^1 and 2^19^1 energy levels is quite large. For nitric acid, seven of its nine vibrational modes correspond to vibrational energies lower than ν_2 . During the computation of energy levels of the 4^1 and 3^1 bright vibrational states at 1303.072 and 1326.186 cm^{-1} [8], four dark states (6^2 , 9^3 , 5^19^1 , and 7^18^1) were identified as responsible for strong perturbations observed during the investigation of the ν_4 and ν_3 bands.

As can be seen in Fig. 2, our FTS spectrum is severely overlapped with lines from CO_2 in the 4.25 μm region, preventing pursuit at a very extended level of the analysis of the $\nu_2+\nu_6$ band. Because this analysis is not extended, identifying the dark states responsible for the observed resonances is not possible.

On the other hand, during the investigation of the $\nu_2+\nu_9$ and $\nu_2+\nu_9-\nu_9$ bands, we could identify that large amplitude torsional splittings are responsible for part of the observed resonances. In the 2^19^1 excited state, this splitting is quite large ($^{29}\Delta = 2 \times E_0^{\varphi 0} \approx 0.045 \text{ cm}^{-1}$), compared to the corresponding values in the 9^1 and 9^2 excited state ($^9\Delta = 2 \times E_0^{\varphi 0} \approx 6 \times 10^{-5} \text{ cm}^{-1}$ [17] and $^{99}\Delta = 2 \times E_0^{\varphi 0} \approx 0.0028 \text{ cm}^{-1}$ [19], respectively). More explicitly, this splitting in 2^19^1 is only slightly weaker than the splitting observed in the 9^3 excited state ($^{999}\Delta = 2 \times E_0^{\varphi 0} \approx 0.059 \text{ cm}^{-1}$) which is surprising.

One possible explanation is that the 2^19^1 energy levels are mixed through a vibration – rotation resonance with those from a dark state located nearby. As this would affect globally all the 2^19^1 levels, the resonance must be mainly of anharmonic type, and the dark state responsible for the perturbations must be of A'' symmetry and involve a high excitation in the ν_9 vibrational state.

We identify two possible candidates, the 5^19^3 and 9^5 dark states. It is difficult to foresee the positions of these dark states since our predictions are based on (large) extrapolations from experimental data. In addition, a strong Fermi resonance coupling together the $5^1 \Leftrightarrow 9^2$ [19] and $5^19^1 \Leftrightarrow 9^3$ [8] energy levels exists.

20/09/2021

For the of 5^19^3 state, we propose a (very) crude estimate of its position at $E_{5999} \approx 2179 \text{ cm}^{-1}$, with an uncertainty not better than $\sim 40 \text{ cm}^{-1}$. This value is based on the positions of the 9^1 , 5^1 , 5^19^1 , 9^1 , 9^2 , and 9^3 states [15]. For this dark state, the torsional splitting is assumed to originate only from its large excitation in ν_9 (9^3) because ν_5 is a low amplitude mode of vibration. In such conditions, the $\%(2^19^1/5^19^3)$ percentage mixing ratio of the 2^19^1 energy levels with those of the (dark) 5^19^3 state should be in the ratio of the observed splittings in 2^19^1 and in 5^19^3 , more explicitly:

$$\%(2^19^1/5^19^3) \approx (0.045 \text{ cm}^{-1} / 0.059 \text{ cm}^{-1}) \approx 76 \% \quad \text{Eq. (12)}$$

This is a problem because this mixing ratio (main \leftrightarrow dark) should not exceed the 50% boundary limit, and it proves that 5^19^3 cannot be the “only” dark state responsible for the observed torsional splittings in 2^19^1 .

The other candidate is the 9^5 state, for which we predicted the positions of the two torsional subcomponents at 2018.8 and 2027.2 cm^{-1} , respectively. This calculation, for which the estimated accuracy is not better than $\sim 200 \text{ cm}^{-1}$, is performed by solving the Mathieu’s equation of the HNO_3 torsional potential [14, 15]. However, one can be reasonably more confident in our assessment of the torsional splitting in the 9^5 state, which is estimated at $\sim 8 \text{ cm}^{-1}$ ($\pm 1 \text{ cm}^{-1}$). It is thus presumed that the 9^5 state is involved, at least partially, in the observed torsional splittings in 2^19^1 .

Going further in the analysis is therefore difficult. We hope that future ab initio calculations like those performed in Refs. [17, 23, 24, 25, 26, 27] will provide more precise explanations.

V Conclusion

We have performed the first investigations of the $\nu_2+\nu_7$ and $\nu_2+\nu_9$ bands, and the first identification of the $\nu_2+\nu_6$ band of nitric acid. For the $\nu_2+\nu_7$ band that seems unperturbed, results are excellent. The investigation of the $\nu_2+\nu_9$ band was combined with the analysis of the $\nu_2+\nu_9-\nu_9$ hot band and, in this way, we observed an unexpected large torsional splitting in the 2^19^1 energy levels. Our calculations reproduce satisfactorily these large amplitude effects for the first rotational energy levels of 2^19^1 . However additional resonances due to dark states

20/09/2021

were observed which could not be accounted for. Finally, only a partial investigation was done for the $\nu_2+\nu_6$ band which is highly perturbed. We used the line position parameters achieved in this work for the 2^{19}_1 , 2^{17}_1 , and 2^{16}_1 energy levels to generate the linelists for the $\nu_2+\nu_9-\nu_9$, $\nu_2+\nu_7-\nu_7$, and $\nu_2+\nu_6-\nu_6$ hot bands that appear together with the ν_2 cold band of HNO_3 in the 5.8 μm spectral region.

The lists of the assigned lines for the $\nu_2+\nu_6$, $\nu_2+\nu_7$, $\nu_2+\nu_9$, $\nu_2+\nu_9-\nu_9$ bands (archive_1), the synthetic spectra (line positions and intensities) of the $\nu_2+\nu_6$, $\nu_2+\nu_7$, $\nu_2+\nu_9$ bands (archive_2), and the results of the calculations (archive_3) are given in the Supplementary data of this article. As far as the 5.8 μm region is concerned, the linelists for the $\nu_2+\nu_9-\nu_9$, $\nu_2+\nu_7-\nu_7$, and $\nu_2+\nu_6-\nu_6$ hot bands together with the updated ν_2 linelist are also available in the supplementary data of Ref. [3].

ACKNOWLEDGMENTS

The authors acknowledge support from ANR (project QUASARS-19-CE29-0013-01) and Synchrotron SOLEIL (projects 99180072 and 99200018). We also thank the CNES (Centre National d'Etudes Spatiales) for financial support through the IASI-NG satellite project. We thank Geoffrey Toon (Jet Propulsion Laboratory, California Institute of Technology, Pasadena California, USA) for comments on the manuscript and for HNO_3 spectroscopy evaluations.

20/09/2021

References

- [1] I.E. Gordon, L.S. Rothman, C. Hill, R.V. Kochanov, Y. Tana, P.F. Bernath, M. Birk, V. Boudon, A. Campargue, K.V. Chance, B.J. Drouin, J.-M. Flaud, R.R. Gamache, J.T. Hodges, D. Jacquemart, V.I. Perevalov, A. Perrin, K.P. Shine, M.A. Smith, J. Tennyson, G.C. Toon, H. Tran, V.G. Tyuterev, A. Barbe, A.G. Csaszar, V.M. Devi, T. Furtenbacher, J.J. Harrison, J.M. Hartmann, A. Jolly, T.J. Johnson, T. Karman, I. Kleiner, A.A. Kyuberis, J. Loos, O.M. Lyulin, S.T. Massie, S.N. Mikhailenko, N. Moazzen-Ahmadi, H. Muller, O.V. Naumenko, A.V. Nikitin, O.L. Polyansky, M. Rey, M. Rotger, S.W. Sharpe, K. Sung, E. Starikova, S.A. Tashkun, J. Vander Auwera, G. Wagner, J. Wilzewski, P. Wcisło, S. Yuh and E.J. Zak, *The HITRAN2016 molecular spectroscopic database*. J. Quant. Spectrosc. Radiat. Transf. **203**, 3–69 (2017).
- [2] N. Jacquinet-Husson, R. Armante, N.A. Scott, A. Chedin, L. Crepeau, C. Boutammine, A. Bouhdaoui, C. Crevoisier, V. Capelle, C. Boone, N. Poulet-Crovisier, A. Barbe, D.C. Benner, V. Boudon, L.R. Brown, J. Buldyreva, A. Campargue, L.H. Coudert, V.M. Devi, M.J. Down, B.J. Drouin, A. Fayt, C. Fittschen, J.-M. Flaud, R.R. Gamache, J.J. Harrison, C. Hill, O. Hodnebrog, S.M. Hu, D. Jacquemart, A. Jolly, E. Jimenez, N. Lavrentieva, A.W. Liu, L. Lodi, O.M. Lyulin, S.T. Massie, S. Mikhailenko, H.S.P. Muller, O.V. Naumenko, A. Nikitin, C.J. Nielsen, J. Orphal, V. Perevalov, A. Perrin, E. Polovtseva, A. Predoi-Cross, M. Rotger, A.A. Ruth, Y. Shanshan, K. Sung, S. Tashkun, J. Tennyson, V.G. Tyuterev, J. Vander Auwera, B. Voronin and A. Maki, *The 2015 edition of the GEISA spectroscopic database*. J. Mol. Spectrosc. **327**, 31–72 (2016).
- [3] A. Perrin, L. Manceron, R. Armante, F. Kwabia-Tchana, P. Roy, D. Doizi, and G.C. Toon. *The 5.8 μm absorption bands for nitric acid ($\text{H}^{14}\text{N}^{16}\text{O}_3$): line positions and intensities for the ν_2 band at 1709.567 cm^{-1} and for its first associated hot bands ($\nu_2+\nu_9-\nu_9$, $\nu_2+\nu_7-\nu_7$, $\nu_2+\nu_6-\nu_6$)*. Molecular Physics, this issue.

20/09/2021

- [4] D.T. Petkie, P. Helminger, B.P. Winnemisser, M. Winnemisser, R.A.H. Butler, K.W. Jucks, F.C. De Lucia. *The simulation of infrared bands from the analyses of rotational spectra: the $2\nu_9-\nu_9$ and $\nu_5-\nu_9$ hot bands of HNO_3* . J. Quant. Spectrosc. Radiat. Transf. **92**, 129–141 (2005).
- [5] J.-M. Flaud, A. Perrin, J. Orphal, Q. Kou, P.-M. Flaud, Z. Dutkiewicz, C. Piccolo. *New analysis of the $\nu_5+\nu_9-\nu_9$ hot band of HNO_3* . J. Quant. Spectrosc. Radiat. Transf. **77**, 355–364 (2003).
- [6] J.-M. Flaud, G. Brizzi, M. Carlotti, A. Perrin, M. Ridolfi. *MIPAS database: Validation of HNO_3 line parameters using MIPAS satellite measurements*, Atmospheric Chemistry and Physics **6**, 5037-5048 (2006).
- [7] L. Gomez, H. Tran, A. Perrin, R.R. Gamache, A. Laraia, J. Orphal, P. Chelin, C.E. Fellows, J.-M. Hartmann. *Some improvements of the HNO_3 spectroscopic parameters in the spectral region from 600 to 950cm^{-1}* . J. Quant. Spectrosc. Radiat. Transf. **110**, 675-686 (2009).
- [8] A. Perrin, *New Analysis of the ν_3 and ν_4 Bands of HNO_3 in the $7.6\text{ }\mu\text{m}$ Region* dx.doi.org/10.1021/jp401979v | J. Phys. Chem. **A117**, 13236–13248 (2013).
- [9] S. Reymond-Laruinaz, M. Faye, V. Boudon, D. Doizi, L. Manceron, *High-resolution Infrared Spectroscopy and analysis of the ν_2/ν_4 bending dyad of Ruthenium Tetroxide*, J. Mol. Spect. **336** 29-35 (2017).
- [10] M. Faye, M. Bordessoule, B. Kanouté, J.-B. Brubach, P. Roy, L. Manceron, *Improved mid infrared detector for high spectral or spatial resolution and synchrotron radiation use*, Rev. Sci. Inst. **87**, 063119 (2016).

20/09/2021

- [11] A. Anantharajah, F. Kwabia-Tchana, L. Manceron, J. Orphal, Jean-Marie Flaud, *New analysis of line positions of the ν_3 bands of $^{35}\text{ClNO}_2$ and $^{37}\text{ClNO}_2$ around 370 cm^{-1}* , J. Quant. Spectrosc. Radiat. Transf. **253**, 107078, (2020)
- [12] W.B. Kay, S.A. Stern S.A. *Phase relations of nitric acid at physicochemical equilibrium*. Ind. Eng. Chem. **47**, 1463-9 (1955).
- [13] C. Chackerian, S.W. Sharpe, T.A. Blake. *Anhydrous nitric acid integrated absorption cross sections: $820\text{--}5300\text{ cm}^{-1}$* . J. Quant. Spectrosc. Radiat. Transf. **81**, 429-441 (2003).
- [14] A. Perrin, J.-M. Flaud, C. Camy-Peyret, B.P. Winnewisser, S. Klee, A. Goldman, F.J. Murcray, R.D. Blatherwick, F.S. Bonomo, and D.G. Murcray. *First analysis of the $3\nu_9\text{--}\nu_9$, $3\nu_9\text{--}\nu_5$ and $3\nu_9\text{--}2\nu_9$ bands of HNO_3 : torsional splitting in the ν_9 vibrational mode*, J. Mol. Spectrosc. **166**, 224-243 (1994).
- [15] A. Perrin. *Recent progress in the analysis of HNO_3 spectra*. Spectrochim. Acta. **A54**, 375-393 (1998).
- [16] A. Perrin, J.-M. Flaud, F. Keller, A. Goldman, R. D. Blatherwick, F. J. Murcray, and C. P. Rinsland. *Analysis of the $\nu_8+\nu_9$ Band of HNO_3 , Line Positions and Intensities, and Resonances Involving the $\nu_6=\nu_7=1$ Dark State*. J. Mol. Spectrosc. **194**, 113-123 (1999).
- [17] D. T. Petkie, P. Helminger, R. A.H. Butler, S. Albert, and F. C. De Lucia. *The millimeter and submillimeter spectra of the ground state and excited ν_9 , ν_8 , ν_7 and ν_6 vibrational states of HNO_3* . J. Mol. Spectrosc. **218**, 127-130 (2003).

20/09/2021

- [18] T.L.Tan, E.C.Looi, K.T. Lua, *Improved Spectroscopic Constants for the ν_2 infrared Band of HNO_3* . J. Mol. Spectrosc. **155**, 420-423 (1992).
- [19] A. Perrin, J. Orphal, J.-M. Flaud, S. Klee, G. Mellau, H. Mäder, D. Walbrodt, M. Winnewisser. *New analysis of the ν_5 and $2\nu_9$ bands of HNO_3 by infrared and millimeter wave techniques: line positions and intensities*. J. Mol. Spectrosc. **228**, 375-391 (2004).
- [20] J.T. Hougen, *A generalized internal axis method for high barrier tunneling problems, as applied to the water dimer*. J. Mol. Spectrosc. **114**, 395-426 (1985).
- [21] L.H. Coudert, J.T. Hougen, *Tunneling splittings in the water dimer: Further development of the theory*. J. Mol. Spectrosc. **130**, 86-119 (1988).
- [22] L.H. Coudert, J.T. Hougen, *Analysis of the microwave and far infrared spectrum of the water dimer*. J. Mol. Spectrosc. **139**, 259-277 (1990).
- [23] K.J. Feierabend, D.K. Havey, M.E. Varner, J.F. Stanton, V. Vaida, *A comparison of experimental and calculated spectra of HNO_3 in the near-infrared using Fourier transform infrared spectroscopy and vibrational perturbation theory*. J. Chem. Phys. **124**, 124323-1-6 (2006).
- [24] C. Gutlé, J. Demaison, H.D. .Rudolph, *Anharmonic Force Field and Equilibrium Structure of Nitric Acid*. J. Mol. Spectrosc. **254**, 99-107 (2009).
- [25] D. Lauvergnat and A. Nauts. *Torsional energy levels of nitric acid in reduced and full dimensionality with ELVIBROT and TNUM*. Phys. Chem. Chem. Phys. **12**, 8405-8412 (2010) | 8405DOI: 10.1039/c001944e.

20/09/2021

- [26] A.I. Pavlyuchko, S.N. Yurchenko, J. Tennyson. *ExoMol molecular line lists: XI The spectrum of nitric acid*. Mon. Not. R. Astron. Soc. 000, 1–5 (2012) Printed 10 July 2015
- [27] A.I. Pavlyuchko, S.N. Yurchenko, J. Tennyson. *A hybrid variational- perturbation calculation of the ro-vibrational spectrum of nitric acid*. J. Chem. Phys. 142, 094309 (2015).

For Peer Review Only

Table 1

Experimental details of the spectra used in this study. The estimated uncertainties are given in parenthesis in the units of the last significant digits.

Spectrum	Spectral range (in cm ⁻¹)	Pathlength (in m)	Pressure (hPa)	Temp (K)	Number of averaged interferograms
FTS262729	2010-2440	16.32 (5)	1.1 (1)	250 (1)	480
FTS2	1650-1750	2.72 (1)	0.027 (1)	296 (1)	368

Table 2

Hamiltonian matrix for the 2^16^1 , 2^17^1 and 2^19^1 vibrational states of HNO_3

Watson-type rotational Hamiltonian (A reduction in I' representation)

$$\begin{aligned} H_W = E_v + & \left[A^v - \frac{1}{2}(B^v + C^v) \right] J_z^2 + \frac{1}{2}(B^v + C^v) J^2 + \frac{1}{2}(B^v - C^v) J_{xy}^2 \\ & - \Delta_K^v J_z^4 - \Delta_{JK}^v J_z^2 J^2 - \Delta_J^v (J^2)^2 - \delta_K^v \{ J_z^2, J_{xy}^2 \} - 2\delta_J^v J_{xy}^2 J^2 \\ & + H_K^v J_z^6 + H_{KJ}^v J_z^4 J^2 + H_{JK}^v J_z^2 (J^2)^2 + H_J^v (J^2)^3 \\ & + h_K^v \{ J_z^4, J_{xy}^2 \} + h_{KJ}^v \{ J_z^2, J_{xy}^2 \} J^2 + 2h_J^v J_{xy}^2 (J^2)^2 + \dots \end{aligned}$$

Torsional operator for the 2^19^1 state

$$\begin{aligned} H^{\text{TORS}} &= \left\{ {}^{\text{IAM}}W^{\text{TORS}}, {}^{\text{IAM}}H_R^{\text{TORS}} \right\} \\ \langle JK'\gamma' | H^{\text{TORS}} | JK''\gamma'' \rangle &= \sum_{K''\gamma''} \left\{ \langle JK'\gamma' | {}^{\text{IAM}}W^{\text{TORS}} | JK''\gamma'' \rangle, \langle JK''\gamma'' | {}^{\text{IAM}}H_R^{\text{TORS}} | JK'\gamma' \rangle \right\} \\ (\text{for } K' \neq 0 \text{ and } K'' \neq 0): \langle JK'\gamma' | {}^{\text{IAM}}W^{\text{TORS}} | JK''\gamma'' \rangle &= \\ (-1)^{K'} \left(\cos((K'+K'')\phi) d_{K',K''}^{(J)}(\theta) + \gamma'' \cos((K'-K'')\phi) d_{K',-K''}^{(J)}(\theta) \right) \\ (\text{for } K' \neq 0, K''=0) \langle JK'\gamma' | {}^{\text{IAM}}W^{\text{TORS}} | JK''=0\gamma''=+1 \rangle &= (-1)^{K'} \sqrt{2} \cos(K'\phi) d_{K',0}^{(J)}(\theta) \\ (\text{for } K'=K''=0) \langle JK'=0\gamma'=+1 | {}^{\text{IAM}}W^{\text{TORS}} | JK''=0\gamma''=+1 \rangle &= d_{0,0}^{(J)}(\theta) \end{aligned}$$

$$\text{with: } \theta = \theta_0 + \theta_J J(J+1)$$

$${}^{\text{IAM}}H_R^{\text{Tors}} = E_0^{\phi\theta} + E_J^{\phi\theta} J^2 + E_Z^{\phi\theta} J_z^2$$

C-type Coriolis resonance within the torsional subcomponents of the 2^19^1 state (v-v diagonal Coriolis operator)

$$h_v^0 \{ J_x, J_z \}$$

1
2
3
4
5
6
7
8
9
10
11
12
13
14
15
16
17
18
19
20
21
22
23
24
25
26
27
28
29
30
31
32
33
34
35
36
37
38
39
40
41
42
43
44
45
46
47
48
49
50
51
52
53
54
55
56
57
58
59
60

For Peer Review Only

Table 3

Part (1) Band centers, rotational and quartic centrifugal constants (in cm^{-1}) for the ground ($v=0$) and the 7^1 , 2^17^1 vibrational states of HNO_3 .

Vibrational state		0^a	7^1^a	2^17^1
E_v			580.303505 ^a	2285.96669(1)
A		0.43399982330	0.434597733	0.432323641(260)
B		0.40360999242	0.403567271	0.402801542(450)
C		0.20883238263	0.206863390	0.206112300(80)
Δ_K	$\times 10^6$	0.2464975	0.200265879	0.2789(140)
Δ_{JK}	$\times 10^6$	-0.15168080	-0.0948235996	-0.12217(190)
Δ_J	$\times 10^6$	0.29708186	0.294057431	0.298520(550)
δ_K	$\times 10^6$	0.2494516	0.263237443	0.266050(240)
δ_J	$\times 10^6$	0.12627092	0.138488674	0.138656(280)
Higher order constants		^a	^a	^b

Part (2): High order centrifugal distortion constants^a

$H_K \times 10^{12}$ 4.11518	$H_J \times 10^{14}$ -1.935	$h_J \times 10^{15}$ 1.151	$l_{KJ} \times 10^{17}$ 2.118
$H_{KJ} \times 10^{12}$ -3.68588	$h_K \times 10^{12}$ 1.7362	$L_K \times 10^{16}$ -1.476	$l_{JK} \times 10^{17}$ -1.9117
$H_{JK} \times 10^{13}$ 9.09863	$h_{JK} \times 10^{14}$ 6.8647	$L_{KKJ} \times 10^{16}$ 1.1861	

^a For the ground and the 7¹ states, the corresponding rotational constants and centrifugal constants are from Petkie et al. [17]. The 7¹ band center is taken from Ref. [15].

^b 2¹7¹ higher order centrifugal constants : fixed to the ground state values [17].

Part (3): Results of the calculation

Number of identified $\nu_2+\nu_7$ lines	677
Number of 2^17^1 infrared levels	381
$0. \times 10^{-3} \leq \delta < 1 \times 10^{-3} \text{ cm}^{-1}$	92.39%
$1 \times 10^{-3} \leq \delta < 3.0 \times 10^{-3} \text{ cm}^{-1}$	7.61%

Table 4

Parameters used in the simulation of the various hot bands. Vib' and Vib'' are the upper and lower state vibrational state. Nb is the number of lines. Sigma min and max are the lower and upper wavenumber range (in cm^{-1}). Band int, Int_{Min} , Int_{Max} are the band intensity, the minimum and maximum value of the line strength (in $\text{cm}^{-1}/(\text{molecule.cm}^{-2})$ at 296 K.

Vib'	Vib''	Band intensity	Nb	Sigma min	Sigma Max	Int Min	Int Max
$\nu_2+\nu_9$	ν_9	0.413E-17	28680	1641.37	1767.50	0.10E-23	0.25E-20
$\nu_2+\nu_6$	ν_6	0.170E-17	17172	1638.16	1759.73	0.10E-23	0.16E-20
$\nu_2+\nu_7$	ν_9	0.237E-17	18705	1638.17	1766.27	0.10E-23	0.22E-20
$\nu_2+\nu_7$	GROUND	0.311E-20	7236	2248.57	2316.20	0.10E-24	0.22D-23
$\nu_2+\nu_9$	GROUND	0.514E-20	7458	2119.32	2203.32	0.10D-24	0.52D-23
$\nu_2+\nu_6$	GROUND	0.131E-20	4757	2321.59	2375.53	0.10D-24	0.10D-23

Table 5. Part (1) : Band centers, rotational and quartic centrifugal constants (in cm^{-1}) for the 6^1 and $2^1 6^1$ vibrational states of HNO_3 .

		6^1 ^a	$2^1 6^1$
E_v		580.303505 ^a	2351.21768(70)
A		0.433840163	0.43086434(780)
B		0.40219502	0.4009665(110)
C		0.2095563	0.2088691671(870)
Δ_K	$\times 10^6$	0.3230785	0.34532 ^c
Δ_{JK}	$\times 10^6$	-0.2644933	-0.28511 ^c
Δ_J	$\times 10^6$	0.3280073	0.33478 ^c
δ_K	$\times 10^6$	0.2602440	0.25920 ^c
δ_J	$\times 10^6$	0.1266811	0.12792 ^c
Higher			
order:		a	b

^a For the ground and the 6^1 states, all rotational constants and centrifugal constants are from Petkie et al. [17]. The 6^1 band center is taken from Ref. [15].

^b 2^16^1 higher order centrifugal constants : fixed to the ground state values [17].

^c All quartic centrifugal distortion constants are extrapolated from those of the ground , 6^1 , [17], and 2^1 [18] vibrational states.

For Peer Review Only

Part (2): Results of the calculation

Number of identified $\nu_2+\nu_6$ lines	207
Number of 2^16^1 infrared levels	120
$0. \times 10^{-3} \leq \delta < 2 \times 10^{-3} \text{ cm}^{-1}$	31.7%
$2 \times 10^{-3} \leq \delta < 6 \times 10^{-3} \text{ cm}^{-1}$	33.3%
$8 \times 10^{-3} \leq \delta < 85 \times 10^{-3} \text{ cm}^{-1}$	35.0%

Table 6

Vibrational Energy, Rotational and Torsional Constants for the 9^1 and 2^19^1 Vibrational States of HNO_3 (in cm^{-1}). Torsional angles in $^\circ$.

		9^1 ^a	2^19^1
E_v		458.228664 ^a	2165.00411(80)
A		0.433598006	0.431555(100)
B		0.400782749	0.399374(180)
C		0.2086520792	0.207894(170)
Δ_K	$\times 10^6$	0.2183544	0.7065(530)
Δ_{JK}	$\times 10^6$	-0.1330057	-0.5787(430)
Δ_J	$\times 10^6$	0.2925377	0.321438(700)
δ_K	$\times 10^6$	0.2421222	-0.0957(260)
δ_J	$\times 10^6$	0.1237489	0.10878(210)
Higher			
order		^a	^b

Torsional parameters (for $v = 2^{19^1}$ only)

	(in °) ^c		(in cm^{-1})
θ_0	0.9736	$E_0^{\phi\theta}$	$2.258(110) \times 10^{-2}$
θ_J	-0.0002600	$E_J^{\phi\theta}$	$-5.10(280) \times 10^{-6}$
ϕ	1.91129	$E_Z^{\phi\theta}$	$-2.828(560) \times 10^{-5}$
		h_{xy}	$-4.4920(470) \times 10^{-3}$

Part (3): Results of the calculation

Number of identified lines	887 306 ($\nu_2 + \nu_9 - \nu_9$) and 578 ($\nu_2 + \nu_9$)
Number of 2^{19^1} infrared levels ^d	517
$0. \times 10^{-3} \leq \delta < 2 \times 10^{-3} \text{ cm}^{-1}$	41.2 %
$2 \times 10^{-3} \leq \delta < 8 \times 10^{-3} \text{ cm}^{-1}$	44.1 %
$8 \times 10^{-3} \leq \delta < 110 \times 10^{-3} \text{ cm}^{-1}$	14.7 %

^a For the 9^1 states, all rotational constants and centrifugal constants are from Petkie et al. [17].

The 9^1 band center is taken from Ref. [15].

^b 2^{19^1} higher order centrifugal constants : fixed to the ground state values [17]

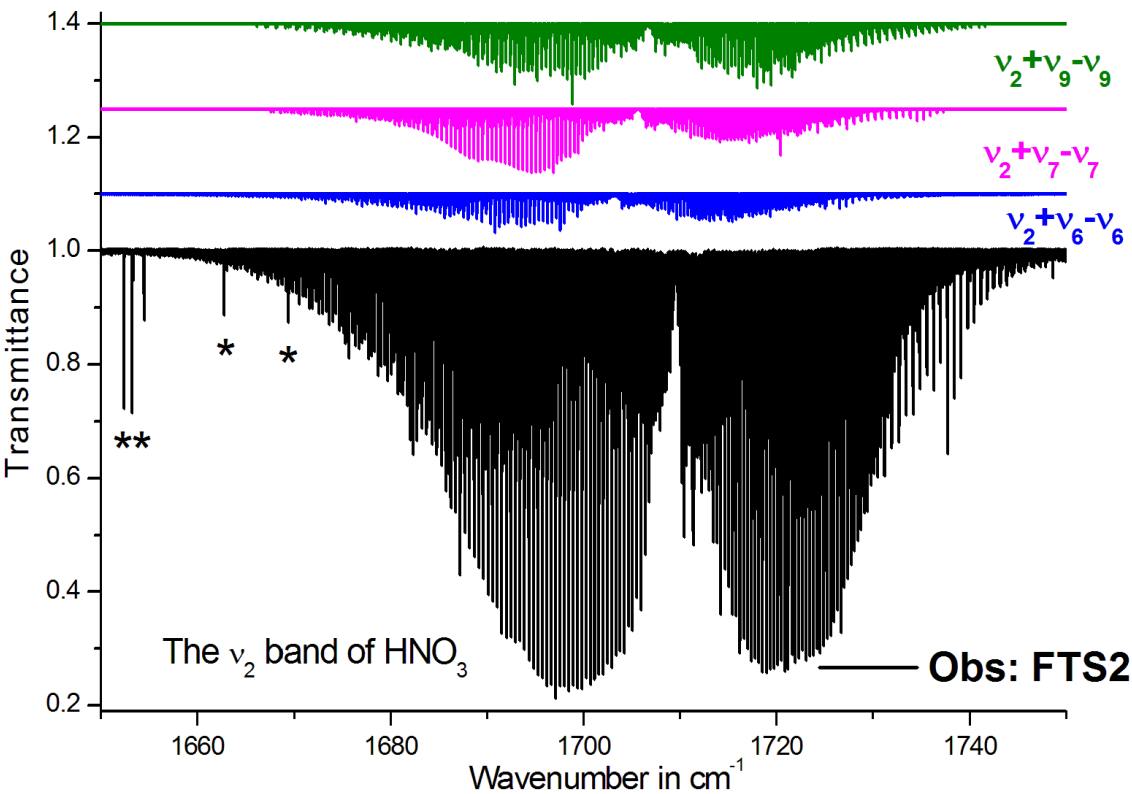
^c The angles involved in the torsional operator are fixed to the values achieved in Ref. [19].

^d $\delta = |E_{\text{Obs}} - E_{\text{Calc}}|$ in cm^{-1} . The 2^{19^1} levels for which δ is larger than $8 \times 10^{-3} \text{ cm}^{-1}$ were not considered in the least squares fit calculation.

1 20/09/2021

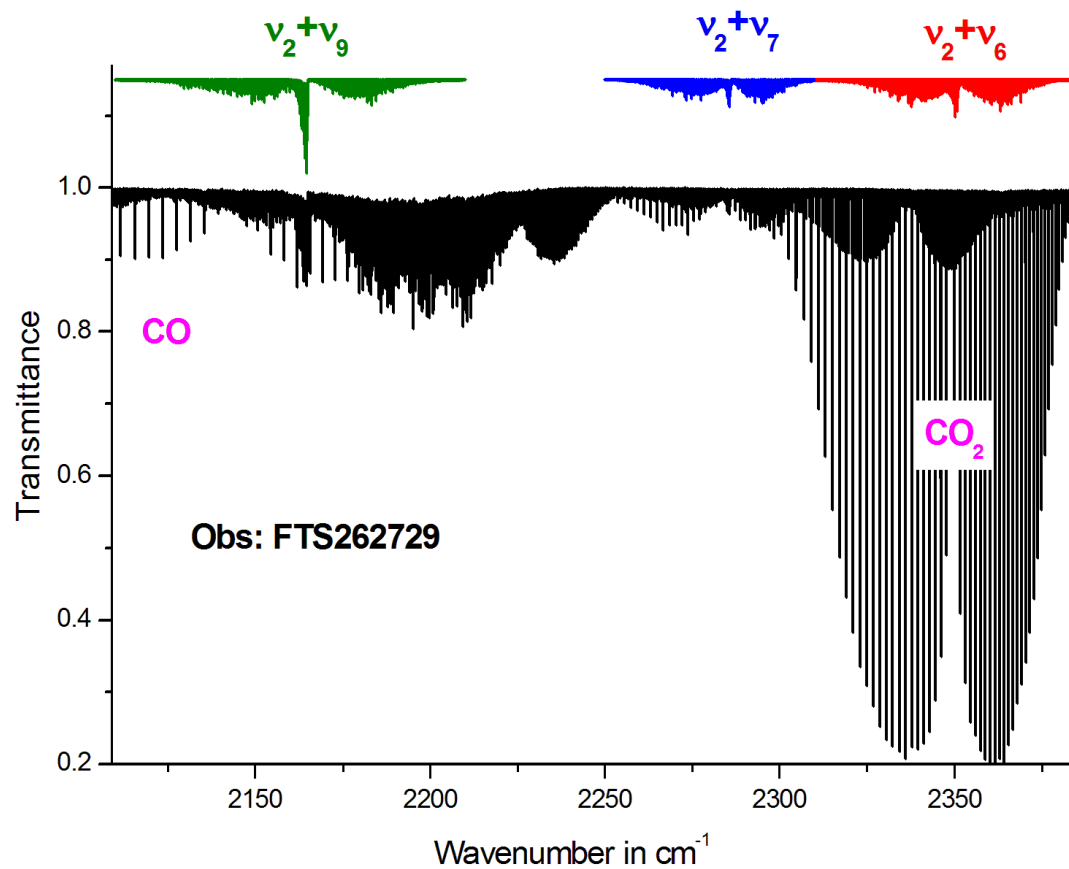
List of Figures

Fig 1: Overview of the FTS2 spectrum (see Table 1), and comparison with the calculated spectra generated in this work for the $\nu_2+\nu_9-\nu_9$, $\nu_2+\nu_7-\nu_7$, and $\nu_2+\nu_6-\nu_6$ bands of HNO_3 . The stars (*) indicate water lines impurities.



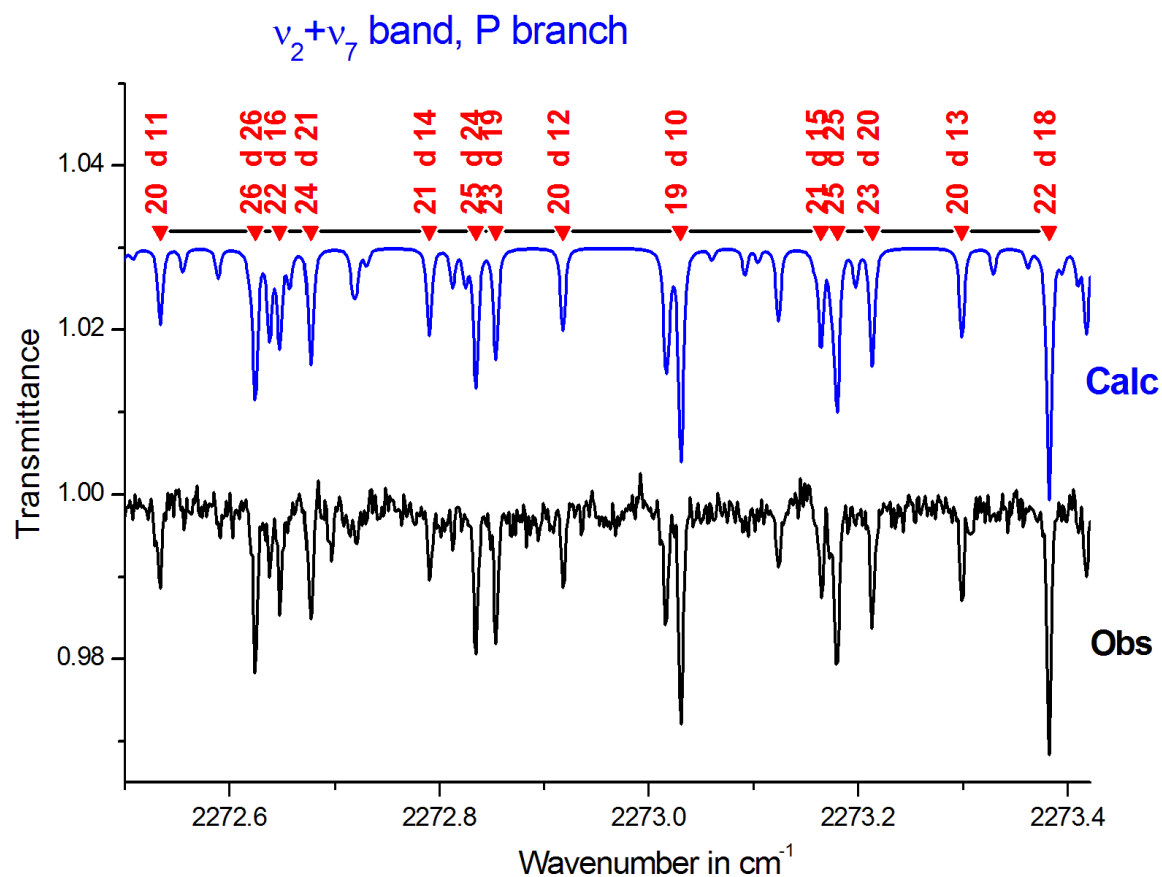
2 20/09/2021

Fig 2: Overview of the FTS262729 spectrum (see Table 1), and comparison with the calculated spectra generated in this work for the $\nu_2+\nu_9$, $\nu_2+\nu_7$, and $\nu_2+\nu_6$ bands of HNO_3 .



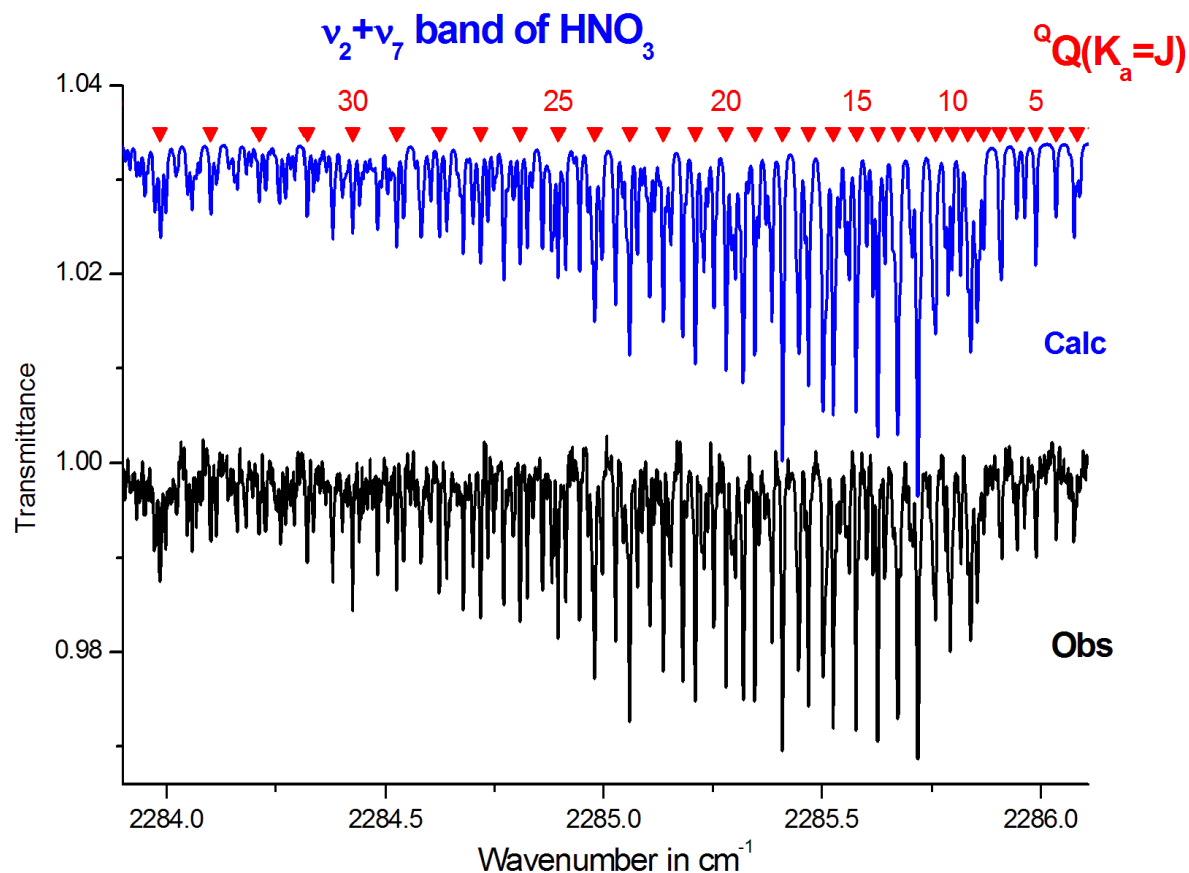
3 20/09/2021

Fig 3: Portion of the P branch part of the $\nu_2+\nu_7$ band in the 2273 cm^{-1} spectral region of the “FTS262729” spectrum recorded in this work and comparison with our calculation . An excellent agreement is observed. Quoted assignments are the $[J, K_a, K_c]$ values in the 2^{17}_1 upper states, and $K_a = d$ stands for degenerated K_a values.



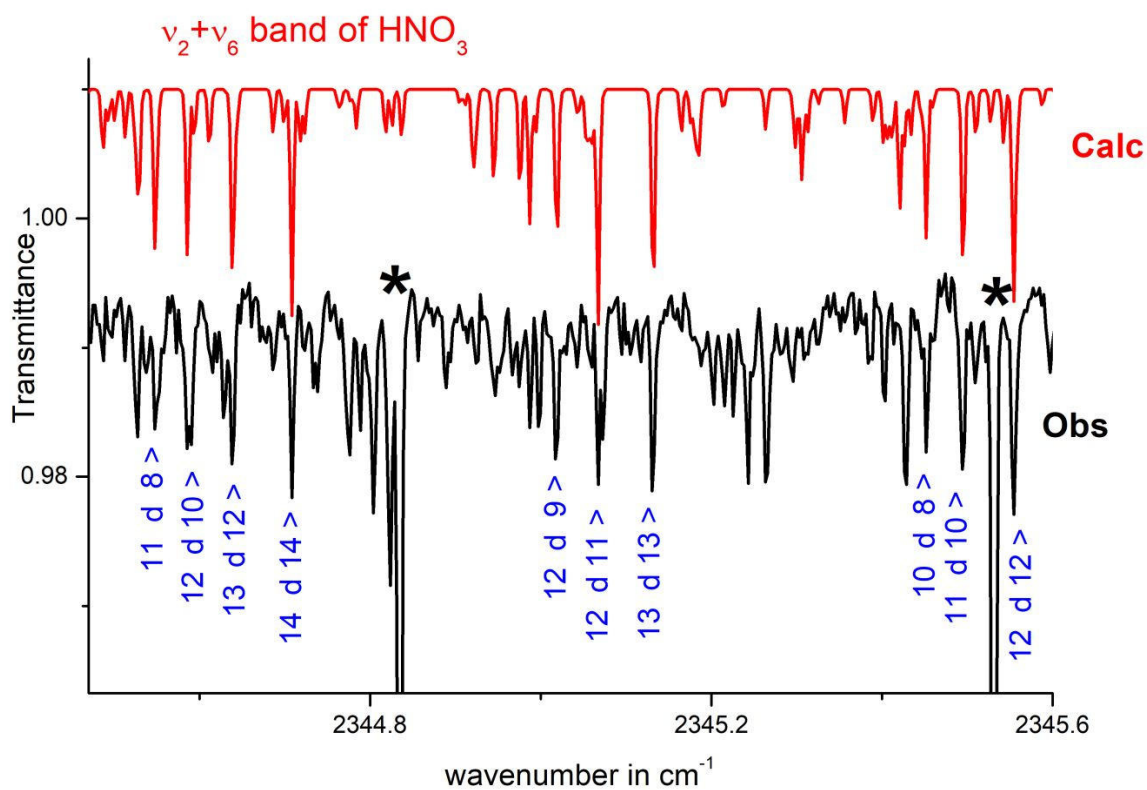
4 20/09/2021

Fig 4: Central part of the A-type Q branch of the $\nu_2+\nu_7$ band of HNO_3 (“FTS262729” spectrum) and comparison with our calculation.



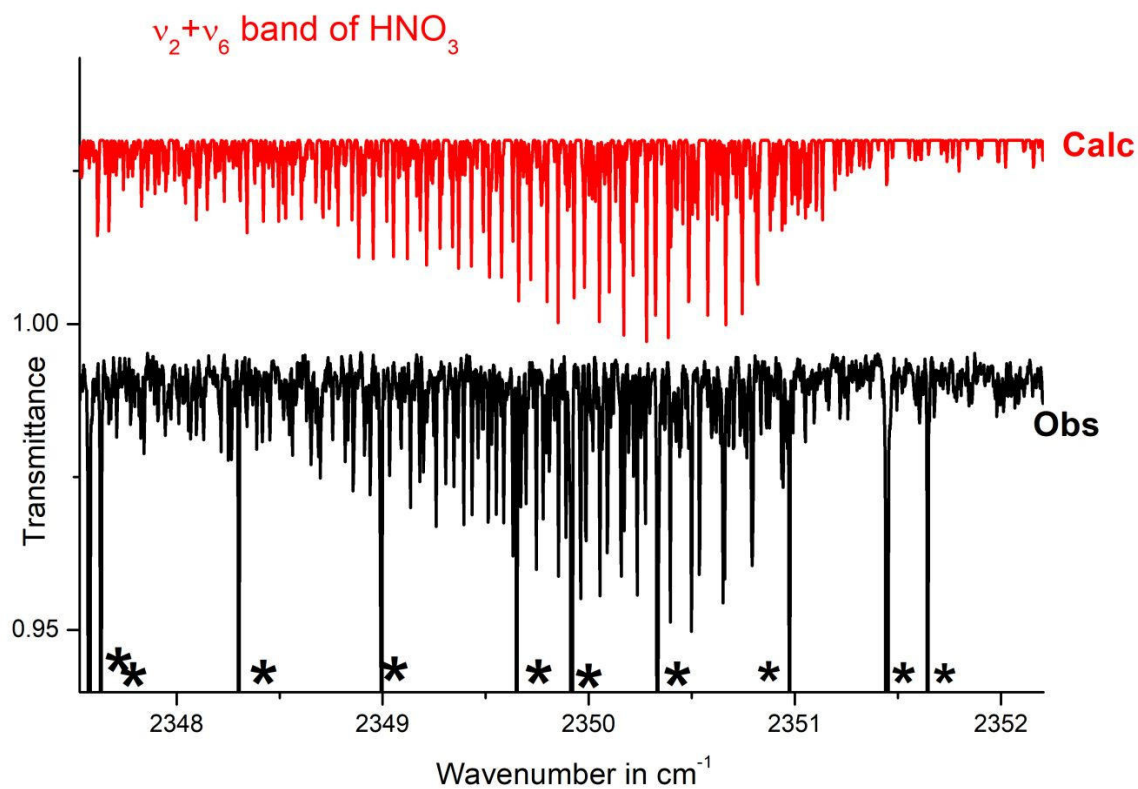
5 20/09/2021

Fig 5: Portion of the P branch of the $\nu_2+\nu_6$ band of HNO_3 in the 2345 cm^{-1} region ("FTS262729" spectrum) and comparison with our calculation. Quoted assignments are in the 2^{16^1} excited states. Lines belonging to CO_2 impurity are also clearly observable in this spectral region (see stars).



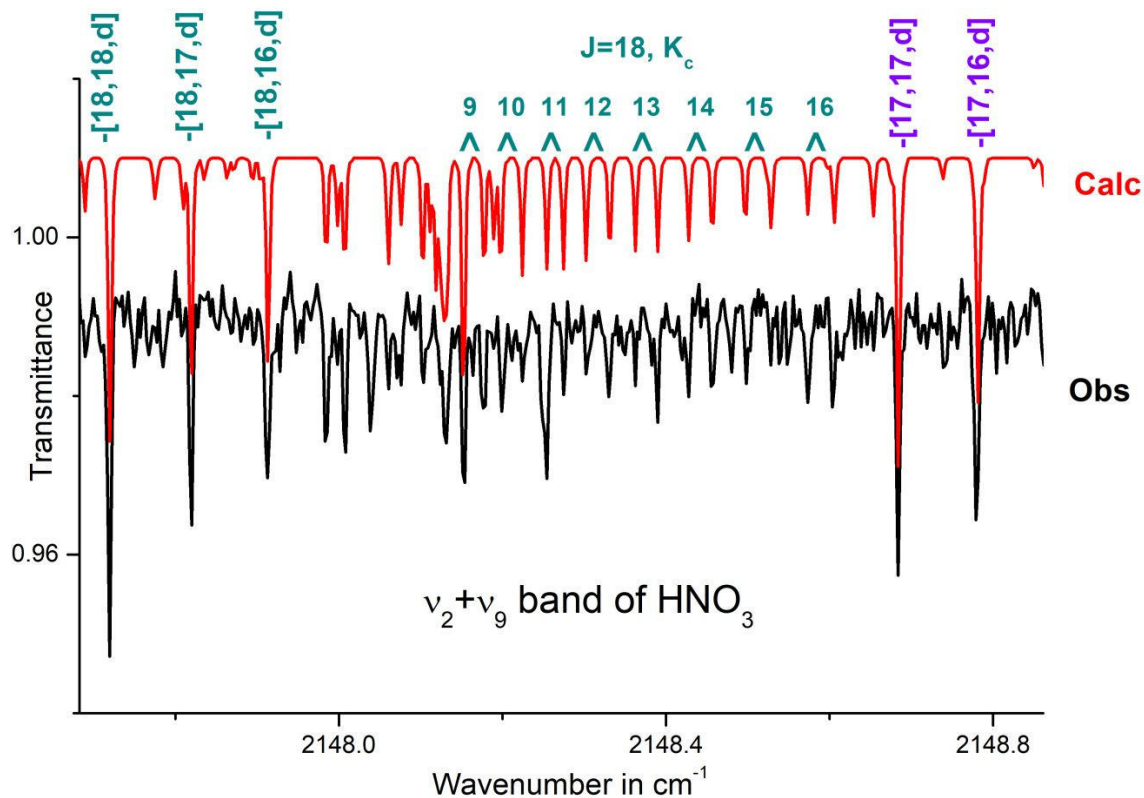
6 20/09/2021

Fig 6: Portion of the Q branch of the $\nu_2+\nu_6$ band of HNO_3 in the 2350 cm^{-1} region in the “FTS262729” spectrum recorded in this work and comparison with our calculation. Strong lines from the $\text{CO}_2\ \nu_3$ band are quite observable in the observed spectrum (see stars).



7 20/09/2021

Fig 7: Portion of the P branch part of the $\nu_2+\nu_9$ band in the 2148.2 cm^{-1} spectral region of the FTS262729 spectrum and comparison with our calculation. Strongest lines involve $[J, K_a, K_c]$ values in the 2^{19}_1 upper state for very high K_a values (K_c is degenerated) for $J = 18$ and $J = 17$. The identified weaker lines involve low K_a values and $J = 18$, and the torsional ($K_a = J - K_c \leftrightarrow K_a = J - K_c + 1$) splitting doublets are indicated by the K_c values in 2^{19}_1 .



8 20/09/2021

Fig 8: Portion of the Q branch part of the $\nu_2+\nu_9$ band in the 2164.6 cm^{-1} spectral region of the FTS262729 spectrum and comparison with our calculation. Quoted assignments are the $[J, K_a, K_c = J]$ values in the 2^{19}_1 upper state for $K_a = 0$ and $K_a = 1$. The torsional splittings ($K_a = J - K_c \leftrightarrow K_a = J - K_c + 1$) are clearly observable.

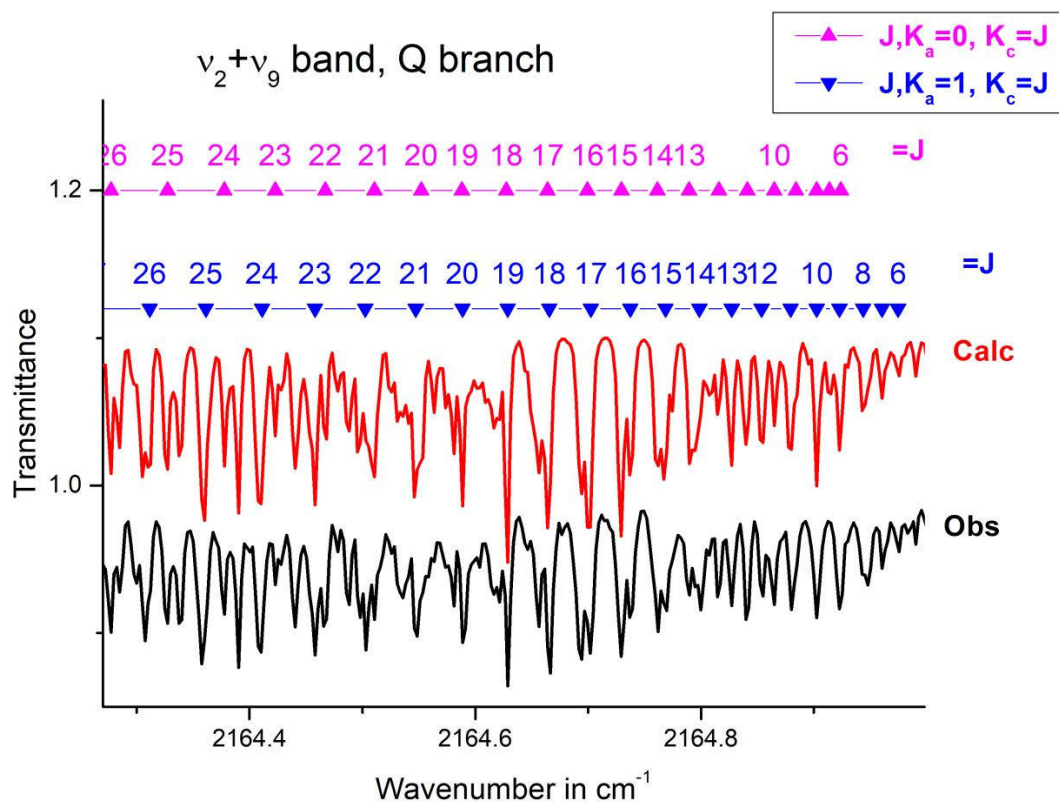
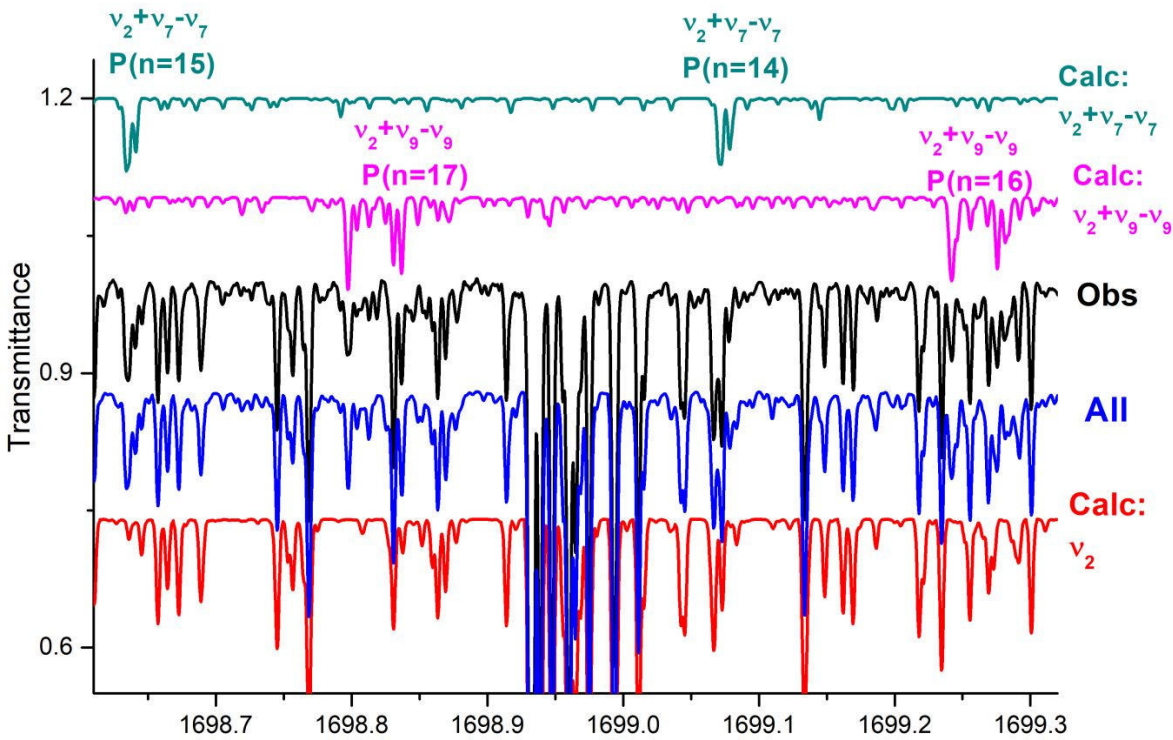
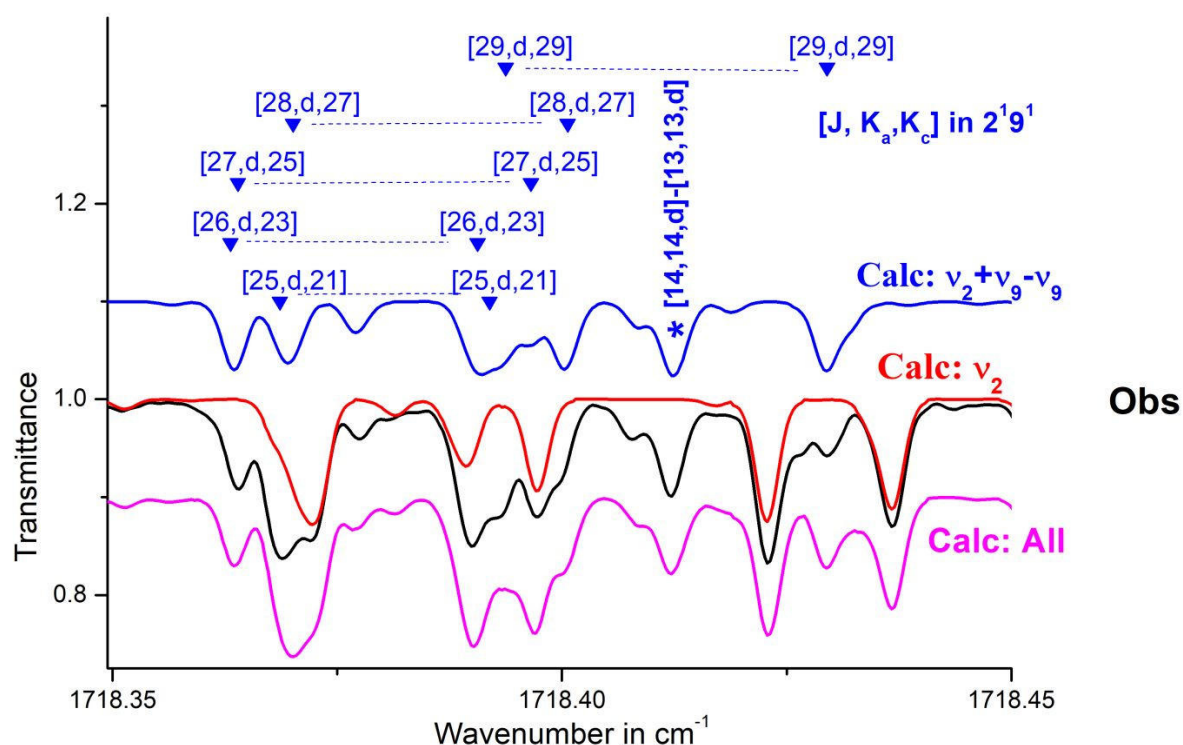


Fig 9: Portion of the HNO₃ spectrum in the 1699 cm⁻¹ spectral region. The “Obs” plot is FTS2 spectrum described in Table 1. The calculated plots are the ν_2 cold band [3], the $\nu_2+\nu_9-\nu_9$ and $\nu_2+\nu_7-\nu_7$ hot bands, and all bands (ν_2 and hot bands). Within those of the P branch of the ν_2 cold band, transitions belonging to several hot bands are observable. Each P(n) cluster groups together lines for which the upper state J and K_c rotational quantum numbers correspond to the same “n = (2 × K_c - J)” value (see text). These clusters have a different shape for the $\nu_2+\nu_9-\nu_9$ and $\nu_2+\nu_7-\nu_7$ hot bands because of the existence of large amplitude torsional splittings in the 2¹9¹ excited state.



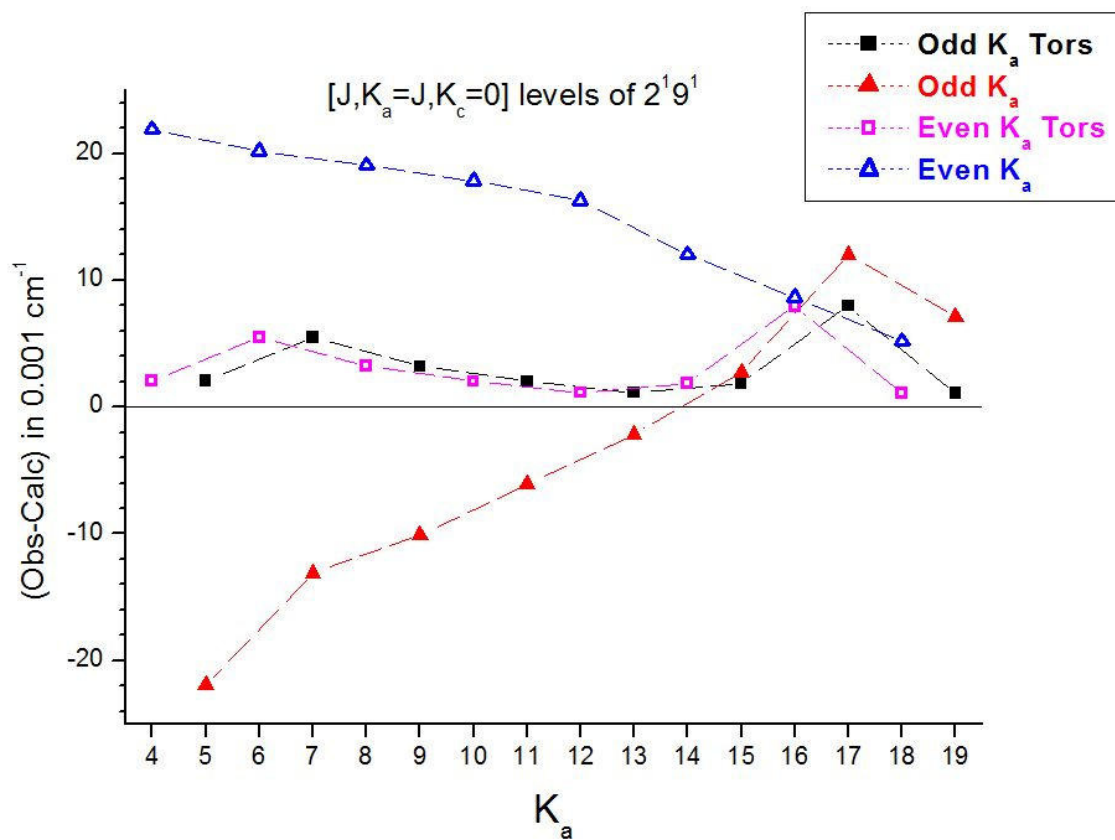
10 20/09/2021

Fig 10: Portion of the HNO_3 spectrum in the 1718.4 cm^{-1} spectral region. The “Obs” plot is FTS2 spectrum described in Table 1, and the calculated plots are the ν_2 cold band [3], the $\nu_2+\nu_9-\nu_9$ hot band, and for all bands (ν_2 and hot bands). A detailed view of the $R(n=29)$ cluster $\nu_2+\nu_9-\nu_9$ hot band, with “ $n = (2 \times K_c - J)$ ”, is presented. Quoted $[J, K_a, K_c]$ assignments are in the $2^1 9^1$ excited state, and the torsional splittings are observable. In addition, the rather strong $[14, 14, d] - [13, 13, d]$ line of $\nu_2+\nu_9-\nu_9$ is identified by a star.



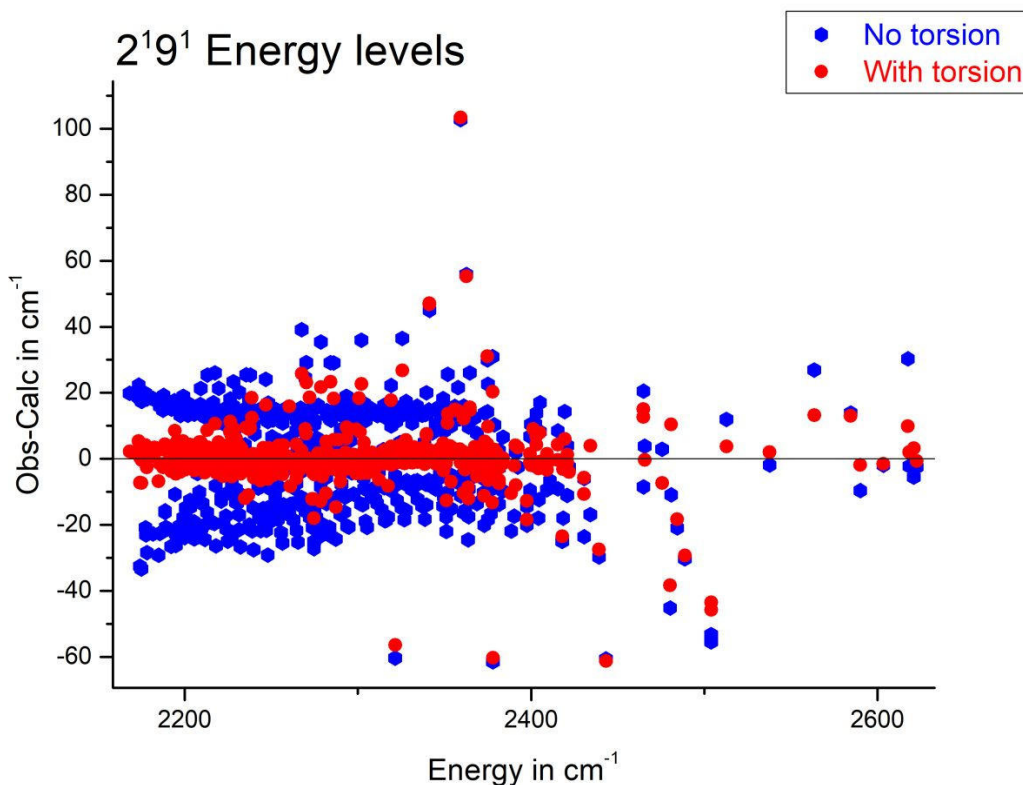
11 20/09/2021

Fig 11: Plot of the (observed – calculated) energy levels for the $[J, K_a = J, K_c = 0]$ of $2^1 9^1$ state for $K_a \leq 19$. The calculations with and without taking into account the torsional splittings are compared.



12 20/09/2021

Fig. 12: Plots of the (observed – calculated) energy levels for the 2^{19}_1 state as a function of the energy level values. The calculations with and without accounting for the torsional splittings are compared. For 2^{19}_1 levels with energies larger than 2350 cm^{-1} , other resonances exist which, unfortunately, could not be taken into account by the current calculation.



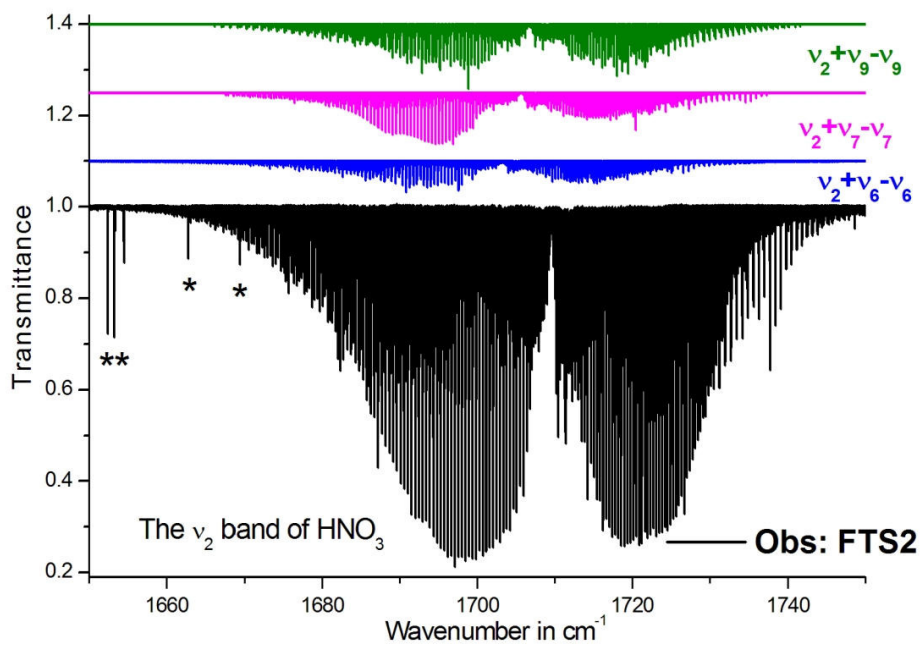


fig 1

279x215mm (150 x 150 DPI)

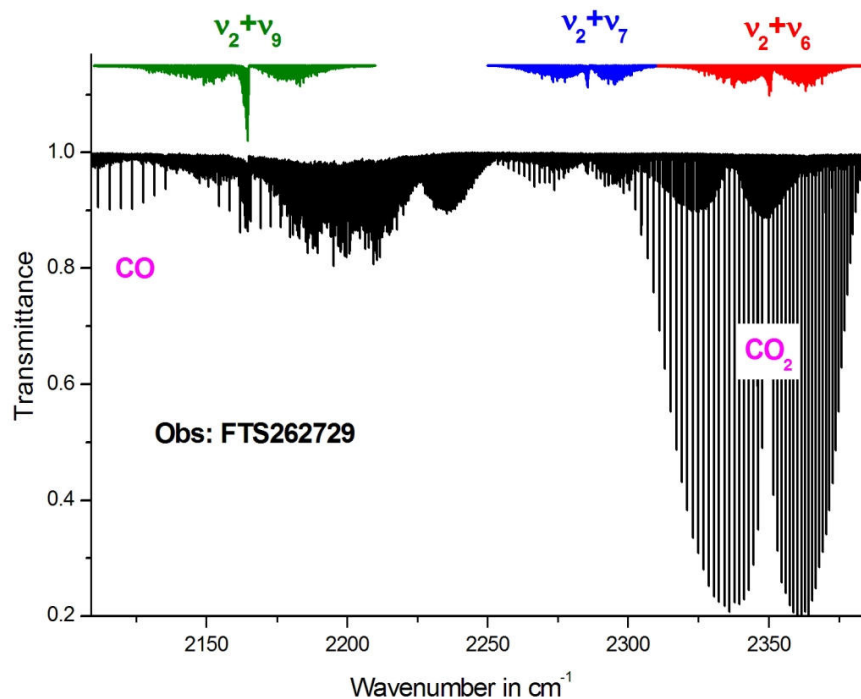


fig 2

279x215mm (150 x 150 DPI)

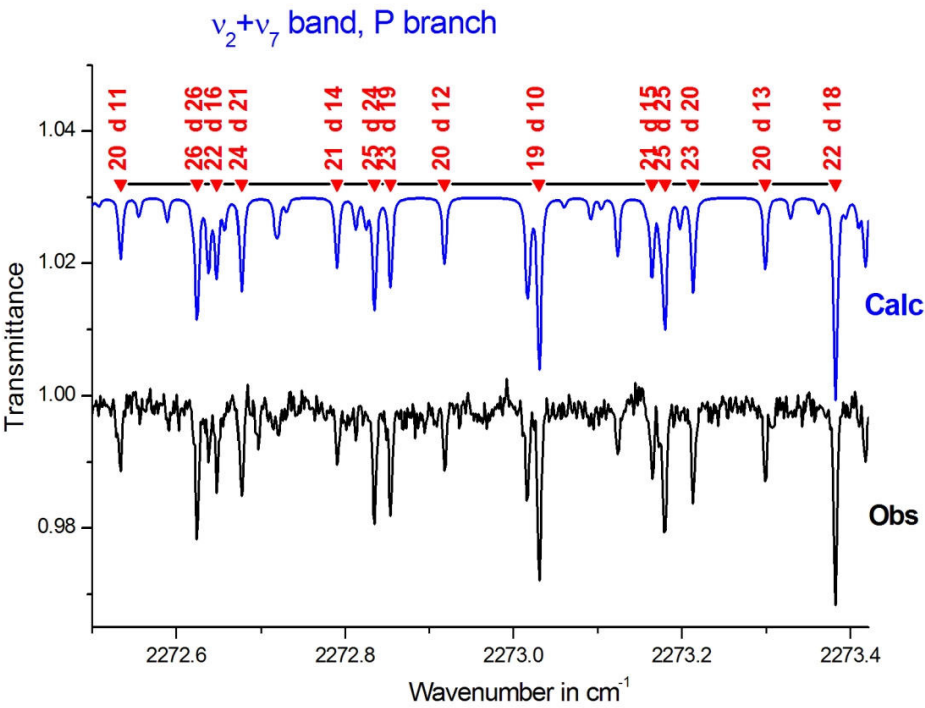


fig 3

279x215mm (150 x 150 DPI)

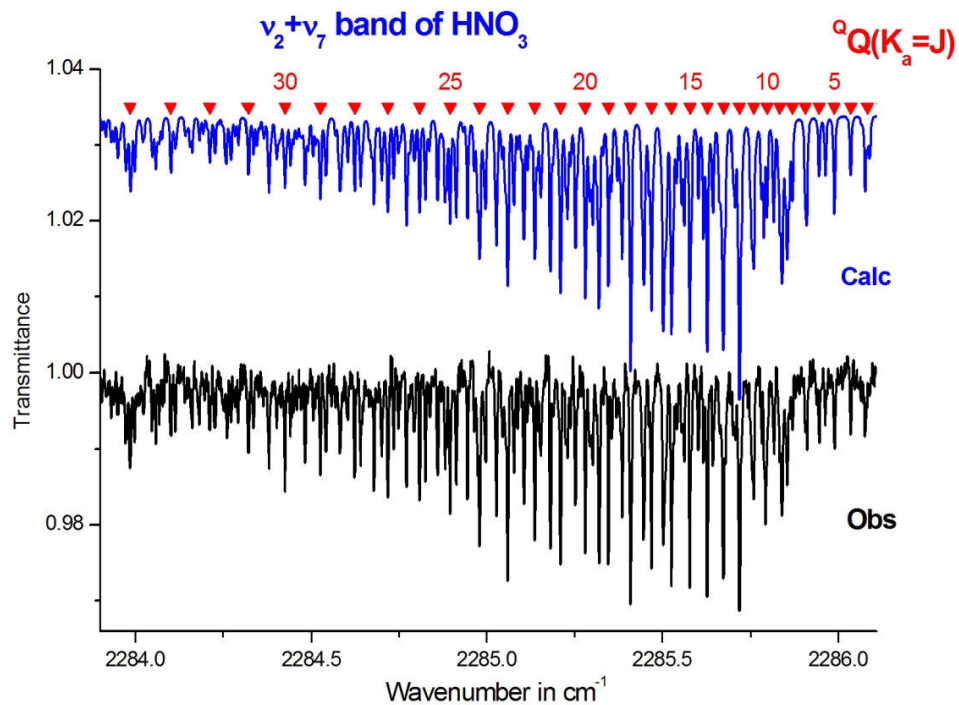


fig 4

279x215mm (150 x 150 DPI)

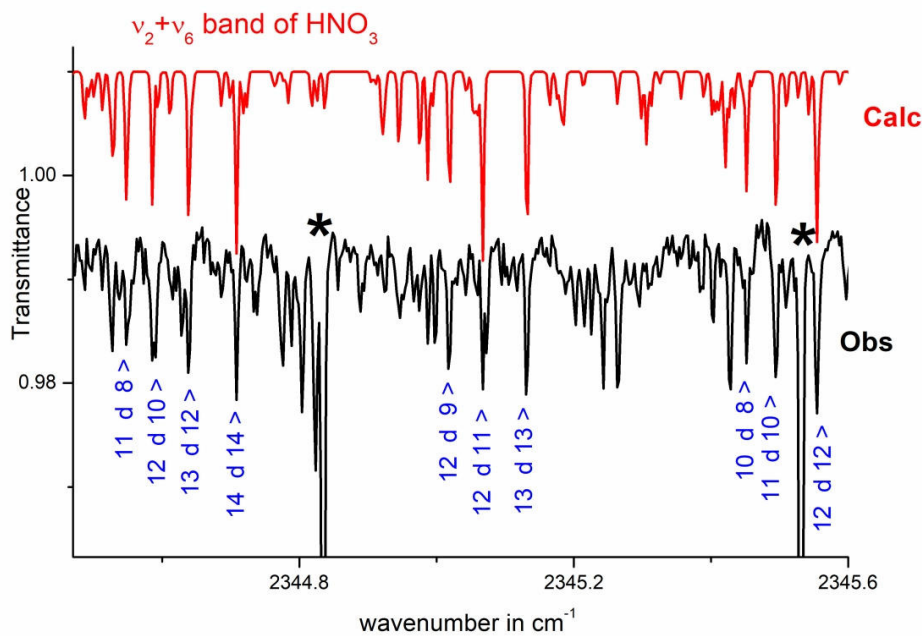


Fig -5 NEW

287x201mm (300 x 300 DPI)

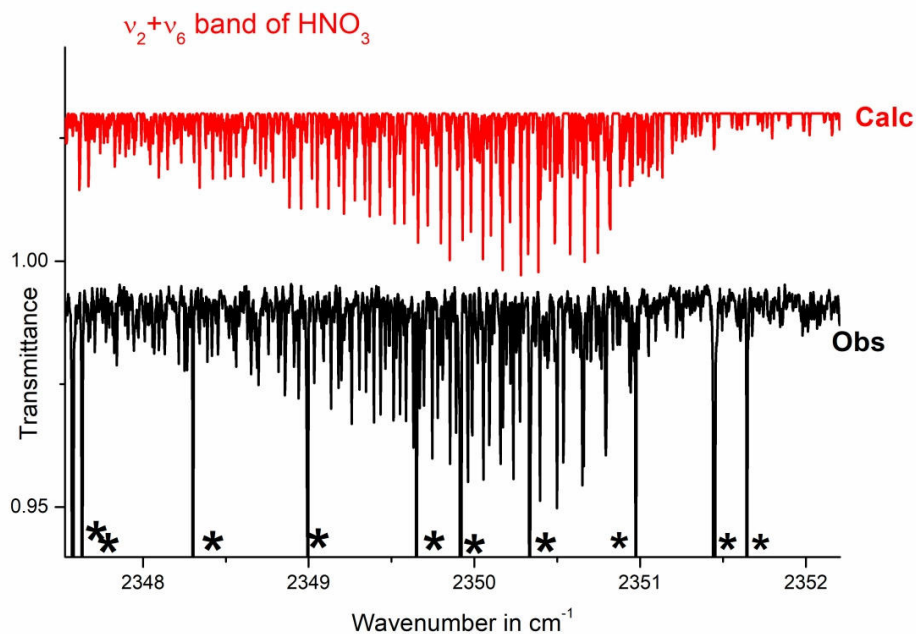


Fig 6 -NEW

287x201mm (300 x 300 DPI)

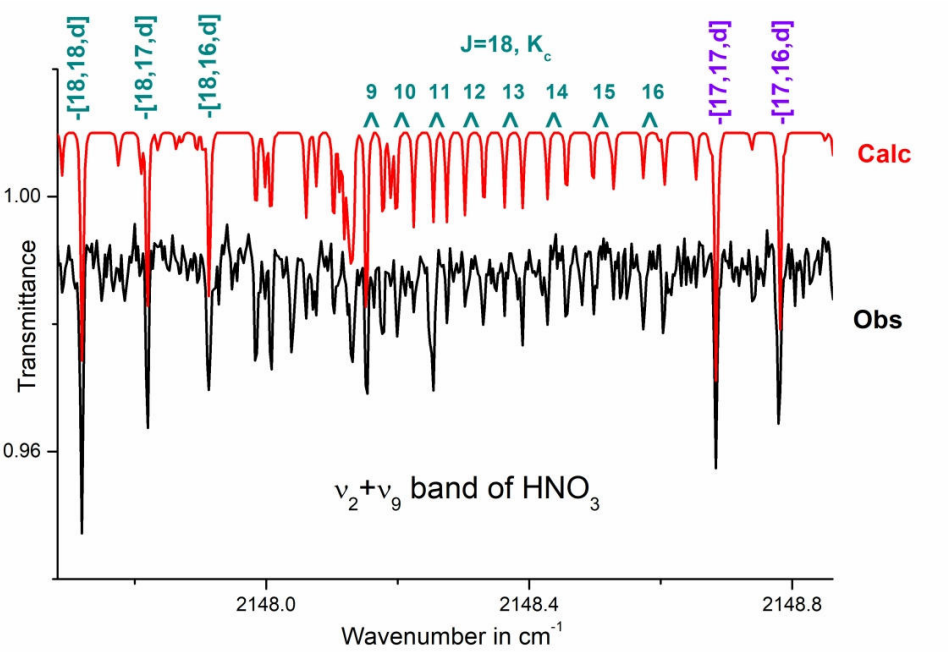


fig 7

287x201mm (300 x 300 DPI)

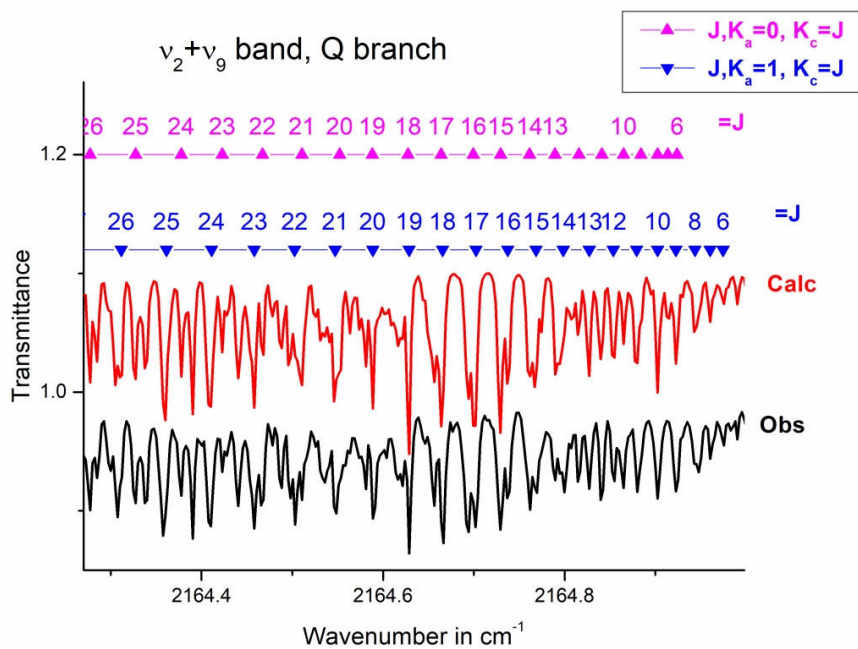


Fig 8

287x201mm (300 x 300 DPI)

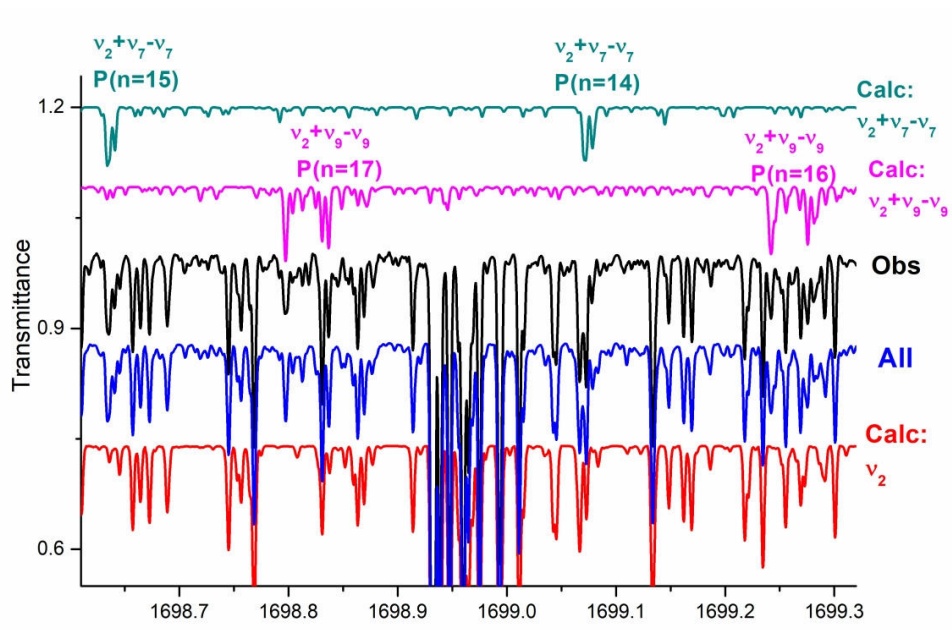


fig 9

287x201mm (300 x 300 DPI)

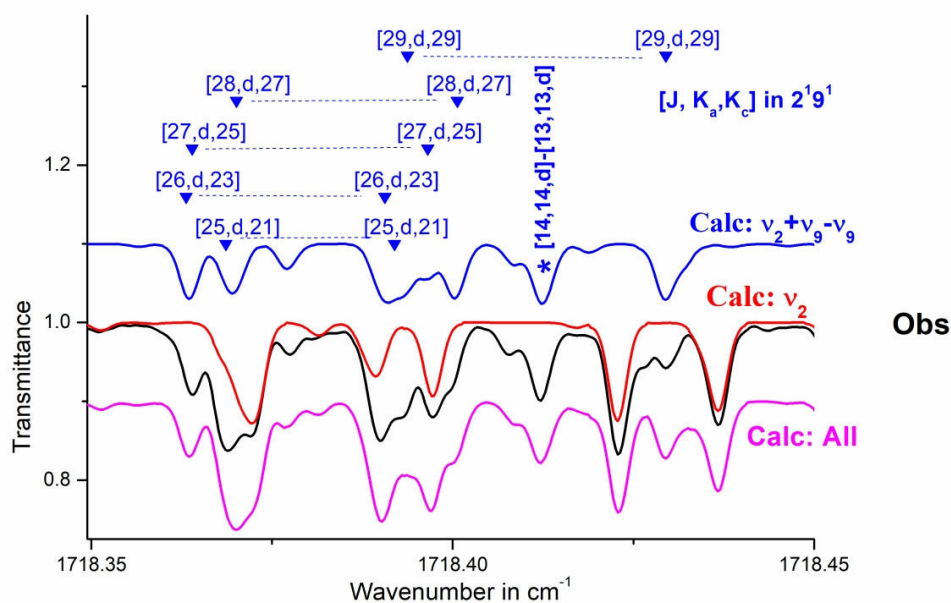


fig 10

287x201mm (300 x 300 DPI)

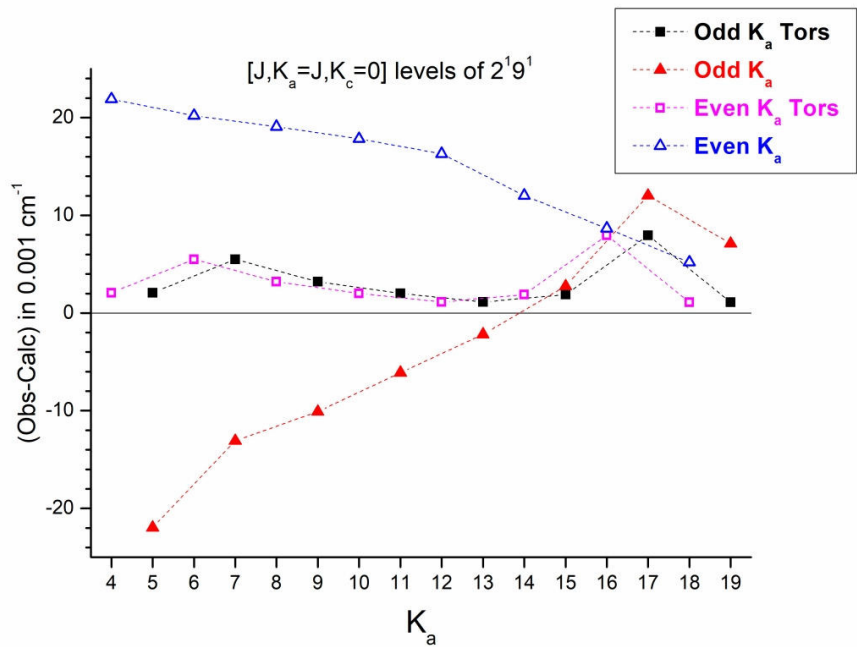


Fig 11

287x201mm (300 x 300 DPI)

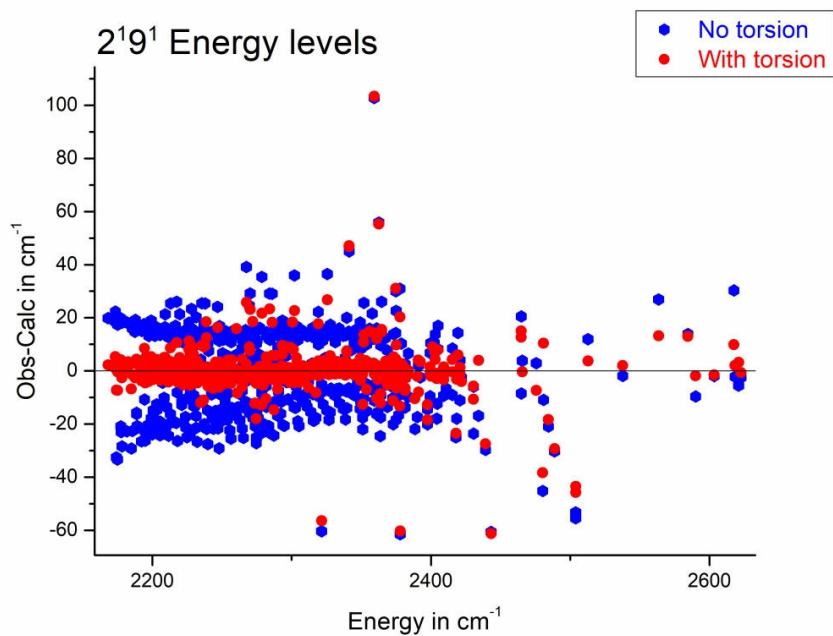


fig 12

287x201mm (300 x 300 DPI)